JOSEPHSON INTERFEROMETRY MEASUREMENTS IN HIGH-T_C GRAIN BOUNDARY JUNCTIONS

BY

WILLIAM K. NEILS

B.S., SUNY Binghamton, 1996
M.S., University of Illinois at Urbana-Champaign, 1999

THESIS

Submitted in partial fulfillment of the requirements
for the degree of Doctor of Philosophy in Physics
in the Graduate College of the
University of Illinois at Urbana-Champaign, 2002

Urbana, Illinois

JOSEPHSON INTERFEROMETRY MEASUREMENTS IN HIGH-T_C GRAIN BOUNDARY JUNCTIONS

William K. Neils, Ph.D.
Department of Physics
University of Illinois at Urbana-Champaign, 2002
Dale J. Van Harlingen, Advisor

We study Josephson junctions formed at grain boundary interfaces in the high-T_c cuprate materials. The inherent properties of these Josephson junctions depend strongly on the pairing symmetry and the electronic structure at the interface and can be used to determine the pairing symmetry as well as the structure of the grain boundary interface. Andreev reflection at the (110) surface in d-wave superconductors leads to the formation of zero-energy quasiparticle surface states. It is predicted that these surface states lead to a suppression of the d-wave order parameter and formation of a subdominant pairing phase with a complex order parameter characterized by broken time-reversal symmetry. A similar phenomenon is predicted to occur in the bulk film near magnetic impurities. Calculations demonstrate that the temperature and magnetic field dependence of the critical current of 45° asymmetric grain boundary Josephson junctions are extremely sensitive to the onset of a complex order parameter. We have measured the critical current behavior of grain boundary junctions of YBCO and BSCCO as well as Ca, Co, Ni, and Pr doped YBCO in an effort to observe the onset a complex order parameter. We see no conclusive evidence for the existence of broken time-reversal symmetry due to a complex order parameter. We do distinct see evidence of second-order Josephson tunneling in a 45° asymmetric BSCCO junction in the form of a critical current peak at zero applied magnetic field. The modulation length of this peak is half that of the others and it exhibits a distinct temperature dependence consistent with a second-order $\sin(2\phi)$ critical current component.

This thesis is dedicated to my beautiful wife Meegan whose love, support, and patience has made it all possible.

Acknowledgments

I would like to thank my research advisor Dale J. Van Harlingen for his guidance, support, and friendship. I also thank the members of the DVH group, both past and present, for their interaction and support in all aspects of my lab work, especially Brian Yanoff, Britton Plourde, Joseph Hilliard, and Tony Bonetti. Their counsel proved invaluable for overcoming many obstacles in my work. I would also like to thank James N. Eckstein, Laura H. Greene, Jochen Mannhart, and their respective groups, whose members are to numerous to mention, for fruitful discussions and for providing me with numerous samples used in my research. Thanks also to the staff of the MRL and it's facilities for providing the environment necessary to perform my research.

Secondly, I would like to thank the friends I have made during my stay here for making a denizen of the east coast feel a little more at home. I especially thank Tony Bonetti(again), Trevis Crane, Adele Rousi, Bruce Davidson, Kara Hamelly, and all the members of the Conduction Band.

Lastly, I would like to acknowledge the financial support of the National Science Foundation grant NSF-DMR99-72087 and the Department of Energy grant DEFDG02-96ER45439.

Contents

List of Tables

List of Figures

Chapter 1

Introduction

Superconductors are a special class of materials with characteristics that are directly related to the quantum state of the system. Superconductivity is one of the few instances when quantum mechanical effects are observable in a macroscopic system. The phenomena associated with both high and low temperature superconductivity will be discussed in this chapter and the superconducting order parameter describing the quantum state will be introduced. Several unconventional order parameter symmetries will be outlined and compared to the conventional BCS ground state. The remainder of the chapter will discuss what happens when two superconductors are allowed to weakly couple forming a Josephson junction. Lastly, a quantum interference device utilizing Josephson junctions will be discussed.

1.1 Superconductivity

1.1.1 Phenomenological Approach

Superconductivity was first observed as a disappearance of the electrical resistance in Hg below a critical temperature of 4.15K. This effect was later seen in many other elements at different material dependent critical temperatures with Nb ($T_c = 9.25K$) being the highest. When a magnetic field (below the critical field) was applied to these materials, screening currents expelled the magnetic flux lines and perfect diamagnetism was observed (the

Meissner effect). Superconductivity has now been observed in a wide range of compounds including exotic materials with critical temperatures in excess of 130K.(get ref)

The extraordinary behavior of superconductors is a result of a weak pairing of electrons. Through interactions with the lattice there is a small net attraction between electrons allowing them to form pairs (Cooper pairs in BCS theory). These paired Fermi particles then act effectively as Bose particles and form a superconducting condensate that can be described with a many-particle wave function containing an amplitude and phase[1].

$$\Psi(\mathbf{r}) = |\Psi(\mathbf{r})|e^{i\theta(\mathbf{r})} \tag{1.1}$$

Since this many particle wave function describes particles in the same state, it is useful to identify the probability density $\Psi^*\Psi$ as the effective density of electron pairs, n_p. Here $n_p = \frac{1}{2}n_s$, where n_s is the density of superconducting electrons. Normalizing the wave function in this manner is useful to relate it to observable quantities. This wave function maintains coherence over large distances giving rise to the observable macroscopic phenomena associated with superconductivity. The coherence length, ξ, is a measure of the length scale over which the wave function is constant and is material dependent. ξ can also be interpreted as the average size of the Cooper pairs.

Using the usual formula for the quantum mechanical probability current, the current density in the presence of external fields is given by[2; 3]

$$\Lambda\mathbf{J_s} = -\left(\frac{\hbar}{2e}\nabla\theta + \mathbf{A}\right) \tag{1.2}$$

where we have introduced the London parameter, $\Lambda = m^*/n_p e^{*2}$, and the vector potential, $\mathbf{A}$. Originally, the mass and charge in the London parameter were incorrectly identified as that of the electron. It is now understood that m^* and e^* are the mass and charge of the pairs and n_p is the pair density. The two phenomenological London equations can be deduced from (1.2) by taking the time derivative and the curl.

$$\frac{\partial(\Lambda\mathbf{J_s})}{\partial t} = \mathbf{E} \tag{1.3}$$

$$\nabla \times \Lambda\mathbf{J_s} = -\mathbf{B} \tag{1.4}$$

While these equations are not based on a microscopic theory, they are useful because they describe the spatial and temporal variation of the superconductivity and introduce some useful parameters. Equation (1.3) describes an accelerating supercurrent in the presence of an electric field, **E**. With no driving force, the current density is constant, consistent with a zero-resistance persistent current state. Using (1.4) together with Ampère's law, assuming there are no other currents, yields

$$\nabla^2 \mathbf{B} = \frac{\mathbf{B}}{\lambda_L^2} \tag{1.5}$$

where

$$\lambda_L = \left(\frac{m^*}{\mu_\circ n_p e^{*2}} \right)^{\frac{1}{2}} \tag{1.6}$$

This equation describes the screening current at the edge of the material induced by the magnetic field. The current flows along the surface and causes the applied field to decay in the material over a characteristic length, λ_L. This λ_L is the London penetration depth and is dependent on the strength of the superconductivity through the density of electron pairs, n_p. Near T_c the n_p goes to zero and the penetration depth diverges.

1.1.2 Flux Quantization

A ring of superconducting material can trap flux inside the ring in contrast to a solid piece of superconductor whose flux is completely expelled. The single valued nature of the superconducting wave function demands that the flux trapped be quantized. This can be shown by taking the path integral of (1.2) inside a superconducting ring, as shown in Fig. 1.1. The integral is equal to the change in the phase around the closed path. This phase change must be zero or an integral multiple of 2π for the wave function to be single valued.

$$\oint (\mathbf{A} + \Lambda \mathbf{J_s}) \cdot dl = \frac{\hbar}{2e} n 2\pi \tag{1.7}$$

If the path is significantly far from the edge of the superconductor where there are no screening currents, $\mathbf{J_s} = 0$ and the integral is simply the flux threading the loop.

$$\oint \mathbf{A} \cdot dl = \Phi = n\Phi_\circ \tag{1.8}$$

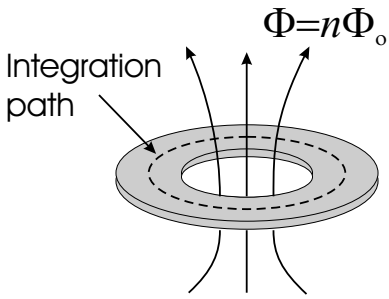

Figure 1.1: A closed ring of superconducting material will trap a quantized amount of flux. The path of integration is show far inside the material where there are no screening currents.

Here $\Phi_\circ = h/2e(= 2 \times 10^{-15})$Wb is the flux quantum and n is an integer. For cases when the superconductor is thin and there are currents at the integration path, it is the entire left half of (1.7) that is quantized. This quantity is referred to as the *fluxoid*. [3]

1.1.3 Type I and Type II Superconductors

The relative size of the coherence length, ξ, and the penetration depth, λ, determine whether a material is a Type I or Type II superconductor. The ratio of the two lengths is known as the Ginzberg-Landau parameter and determines the sign of the free energy term arising from the normal/superconducting interface in the superconductor in the presence of a magnetic field.

$$\kappa = \frac{\lambda}{\xi} \tag{1.9}$$

There are two regimes of large and small κ whose characteristics can be understood in terms of energy cost considerations. For $\lambda \ll \xi$, the energy cost associated with the reduction of the order parameter over a length scale ξ will outweigh the small energy gained by allowing the field to penetrate the superconductor. In this case, the positive surface energy will cause the system to minimize the surface area resulting in the intermediate state. This is a Type I superconductor and is characterized by large normal regions in the presence of a magnetic field. For a Type II material where $\lambda \gg \xi$, a field will penetrate into the superconductor to a length λ resulting in a relatively large gain of energy. However, the order parameter will be suppressed over a small region resulting in a small energy loss.

The resulting negative surface energy will force the system to maximize the surface area and the magnetic field will enter the material in individual vortices with flux $\Phi_\circ$. The crossover ratio between Type I and Type II is $\kappa = 1/\sqrt{2}$ which can be calculated using the Ginsberg-Landau phenomenological theory.

The intermediate state for Type I superconductors characterized by large normal regions with flux penetrating the material is only seen in samples with a non-zero demagnetizing factor. This is a geometric factor that is a measure of how much the applied field is distorted by the superconductor. A sheet of superconductor would have a large demagnetizing factor for fields applied perpendicular to the surface while the factor for a thin rod with field applied along the axis would be near zero. For a non-zero demagnetizing factor the perfect diamagnet Meissner state persists up to an applied field that is reduced from the thermodynamic critical field, $\mathbf{B_c}$.

$$\mathbf{H_{app}} = \frac{\mathbf{B}}{\mu_\circ} - d\mathbf{M} \tag{1.10}$$

In (1.10) d is the demagnetizing factor and $\mathbf{M}$ is the magnetization of the superconductor due to screening. Above this lesser field, the superconductor is in the mixed state where large regions of the material are normal.

In Type II superconductors with zero demagnetizing factor there is a lower critical field, B_{c1}, above which individual vortices enter the material forming the mixed state. These $\Phi_\circ$ flux lines have a characteristic radius λ and increase in density with increasing field. Above an upper critical field B_{c2}, the entire sample switches to the normal state. Similar to the Type I case, a non-zero demagnetizing factor in a Type II superconductor will lower the applied field required for the material to be in the mixed state. The upper critical field is unaffected by this geometric factor.[3; 4]

1.2 Order Parameter Symmetry

All of the equations referenced thus far originate from phenomenological theories and do not provide any insight into the microscopic mechanisms of superconductivity. In 1957

the BCS theory became the first successful microscopic theory which explained the electron pairing in superconductivity through phonon interactions.[5] This theory results in an energy gap, $\Delta_\circ$, in the density of states at the Fermi energy. Later, Gorkov showed that the phenomenological theory of Ginzberg and Landau could be derived from the new theory and that the energy gap is proportional to the wave function of the superconducting state.[6] It is now common to identify the energy gap with the magnitude of the order parameter for the superconducting transition because it is proportional to the wave function and thus has the same symmetry. The order parameter phase is the phase of the many-particle wave function. The magnitude is easily measured in tunnelling spectra where the density of states is probed.

Bardeen, Cooper, and Schrieffer used an isotropic pair potential in their theory which resulted in an isotropic order parameter. This order parameter is called s-wave; an analogy made to the atomic orbital with spherical symmetry. Figure 1.2 a) shows the magnitude and phase of the s-wave order parameter as a function of direction in k-space. This gap function is spherically symmetric and has no relative phase shifts. The BCS theory is believed to describe the pairing mechanism in all the low-temperature superconductors but this isotropic pairing mechanism is inadequate for describing more exotic materials and the (newer) high-temperature cuprates. These superconductors have complex structures with a lower order of crystal symmetry and higher transition temperatures than predicted for phonon mediated coupling. The simpler materials with s-wave pairing symmetry described by the BCS theory are referred to as *conventional* superconductors while the other exotic materials, with order parameters containing phase anisotropy, are called *unconventional*.

The materials used in this study are high-temperature (*unconventional*) cuprate superconductors. It is now widely believed that the cuprate materials undergo spin-singlet pairing with $d_{x^2-y^2}$ symmetry but this was a topic of debate for many years.[7–9] The details of the two cuprate materials, $YBa_2Cu_3O_{7-\delta}$ and $Bi_2Sr_2CaCu_2O_8$, will be discussed in Chapter 2 along with the experimental evidence for the determination of the cuprate order parameter symmetry. The remainder of this section outlines the details of some order parameter

symmetries that were either candidates for the cuprate pairing symmetry or are of interest in the field. Figure 1.2 plots the magnitude and relative phase of the order parameters discussed below.

s-wave Shown in Fig. 1.2 a). This is the standard BCS isotropic pairing symmetry. The magnitude is constant and (ideally) spherically symmetric. There are no relative phase shifts.

anisotropic s-wave Shown in Fig. 1.2 b). The magnitude is asymmetric in k-space with minima along the 45° directions. This order parameter also has no relative phase shift as in the isotropic s-wave symmetry.

$\mathbf{d_{x^2-y^2}}$ Shown in Fig. 1.2 c). The magnitude is asymmetric in k-space with nodes (zero energy gap) along the 45° directions. The order parameter has a relative phase shift of π between orthogonal directions in k-space. This is shown as the solid line on the XY graph plotted along with the magnitude shown as the dashed line. A similar pairing symmetry d_{xy} has the same character rotated by 45°.

$\mathbf{d_{x^2-y^2} + s}$ Shown in Fig. 1.2 d). This is an in-phase (real) admixture of the d-wave and s-wave symmetries. Because the d-wave symmetry has π phase shifts, the s-wave will add to the plus lobes and subtract from the minus lobes resulting in an asymmetric d-wave magnitude. The location of the nodes are shifted away from the $(\overline{1}\,\overline{1}\,0)$ directions but the relative phase shift of π between adjacent lobes is unchanged.

$\mathbf{d_{x^2-y^2} + is}$ Shown in Fig. 1.2 e). The s-wave is added out-of-phase (complex) resulting in the disappearance of the nodes. The order parameter is fully gapped but can still be anisotropic. The relative phase shift is a continuous function of k-space direction where $0 < \phi < \pi$.

$\mathbf{d_{x^2-y^2} + id_{xy}}$ Shown in Fig. 1.2 f). The d_{xy} is added out of phase which results in a completly gapped order parameter but it can still be anisotropic. The relative phase shift now winds continuously as you change direction.

Symmetry	Magnitude and Phase
a) s-wave	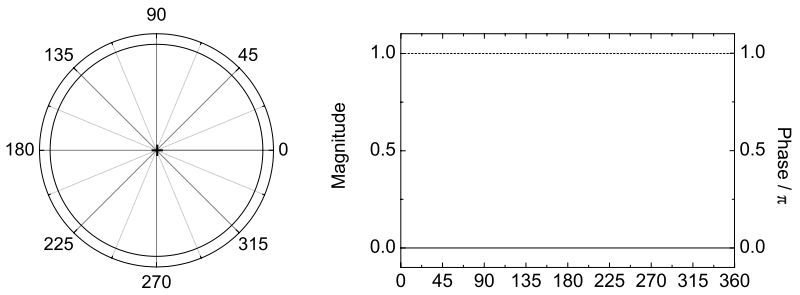
b) anisotropic s-wave	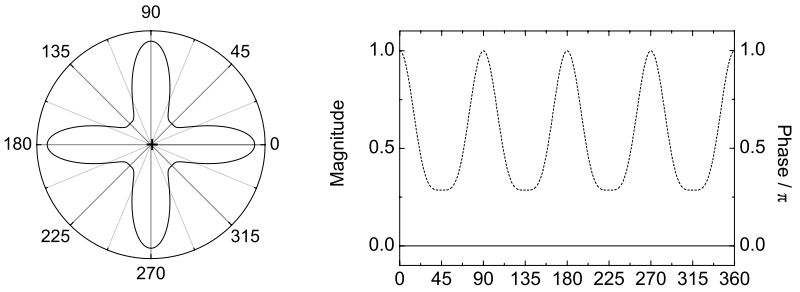
c) d-wave	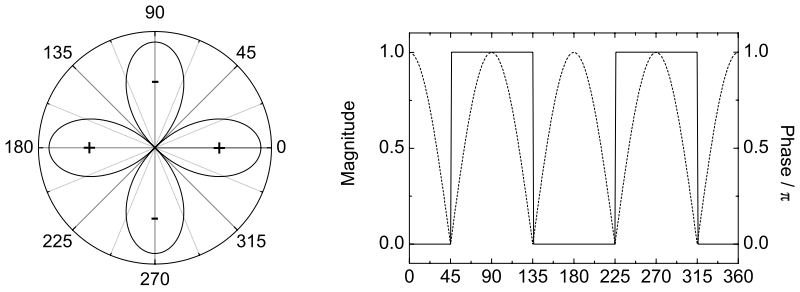

continued on next page

Figure 1.2: A list of possible symmetries for the superconducting order parameter. The radial plot shows the magnitude of the order parameter as a function of angle in k-space. The XY plot shows both the magnitude (dashed line) and the relative phase (solid line) of the order parameter as a function of angle in k-space.

Symmetry	Magnitude and Phase

d) d+s wave

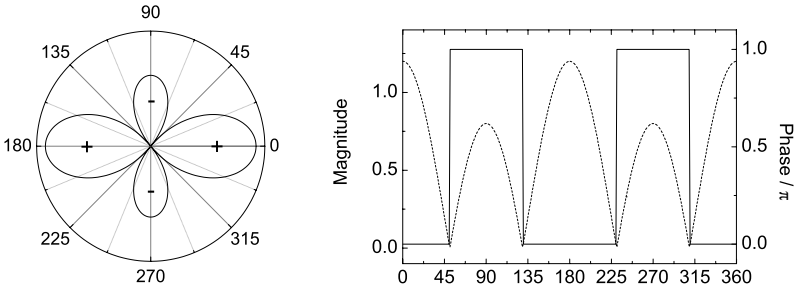

e) d+is wave

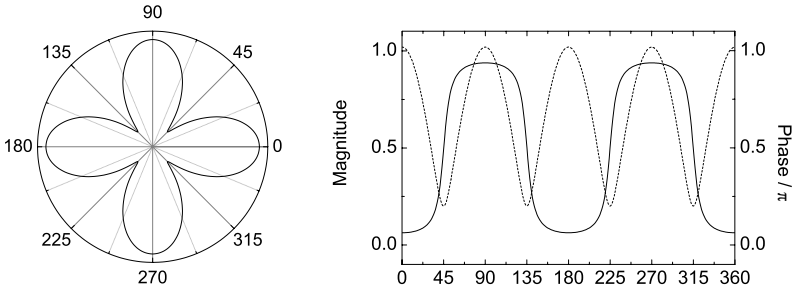

f) d+id wave

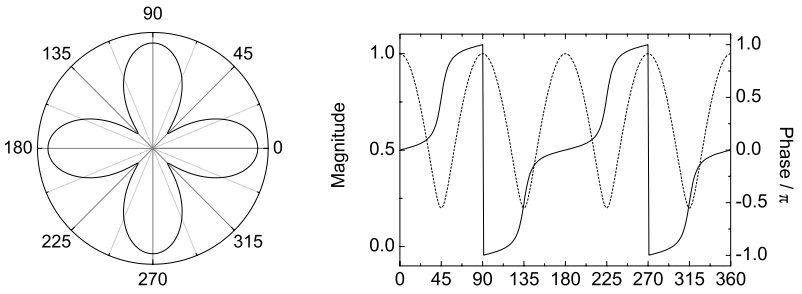

Figure 1.2: (continued) For symmetries with two components, the magnitude of the second component is 20% of the first.

1.3 Weakly Coupled Superconductors: The Josephson Effect

The many-particle wave function, given in (1.1) and derived from the Ginzburg-Landau theory, describes the superconducting order in the system. This function maintains coherence over long distances communicating phase information along any superconducting path. If two superconductors are allowed to weakly interact through a barrier, Cooper pairs can tunnel across producing interesting effects that are dependent on the phase and voltage differences across the barrier.[10] The term Josephson junction is used to describe these weak links. Barrier materials shown to produce Josephson junctions include insulators (SIS), metals (SNS), and constrictions (ScS). This section outlines some of the characteristics of these weak link junctions and describes some useful devices containing them.

1.3.1 Characteristics of Josephson Junctions

Josephson showed[10; 11] that weak-link junctions could carry a *dc* supercurrent at zero voltage up to a maximum value, I_c that depends on the details of the junction. This supercurrent density is generally given by

$$J = J_c(\mathbf{r}) f(\phi) \tag{1.11}$$

where $f(\phi)$ is a function of the phase difference across the junction and $J_c(\mathbf{r})$ is the critical current density which can vary with position in the junction. This function must be 2π periodic because the phase is related to observable quantities that must be single valued. The functional form of f depends on the type of barrier in the junction. For a thin insulating barrier (and for many other cases) $f(\phi) = \sin(\phi)$, but in general, $f(\phi)$ can be any periodic function. ($\sin(\phi)$ will be used in many of the following calculations for simplicity.) Voltages applied to the junction result in an *ac* supercurrent in addition to the *dc* quasi-particle current. The *ac* supercurrent is a result of the time evolution of the phase caused by the applied voltage.

$$\frac{\partial \phi}{\partial t} = \frac{2e}{\hbar} V \tag{1.12}$$

These equations include phase information through the gauge invariant phase ϕ that includes a term due to magnetic fields in the junction.

$$\phi = \Delta\theta - \frac{2e}{\hbar}\int \mathbf{A}\cdot d\mathbf{l} \tag{1.13}$$

Here, $\Delta\theta$ is the gauge dependent phase drop across the junction, $\mathbf{A}$ is again the vector potential, and the integration path traverses the junction across which the phase drop is measured.

Josephson tunneling is directional. Like all other tunneling processes the probability drops off rapidly with increasing angle away from the barrier normal due to an angular dependence of the order parameter decay in the barrier. This produces a tunneling cone centered around the barrier normal whose angular width is determined by the barrier properties. In the case of a normal metal barrier, the tunneling cone is dependent on the barrier thickness, x, and the normal metal coherence length, $\xi(\theta)$. The tunneling matrix element then has the following angular dependence.[12; 13]

$$\tilde{T} \propto \exp\left(-\frac{x}{2\xi(\theta)}\right) \quad \text{where} \quad \xi(\theta) = \frac{2\pi k_B T}{\hbar v_F \cos\theta} \tag{1.14}$$

A thick barrier reduces the tunneling and narrows the tunneling cone. Thus a Josephson junction is most depend on the properties of the order parameter in the k-space direction normal to the barrier and is useful as a directional probe of the superconducting material comprising the junction.

Magnetic Fields

Magnetic fields in the barrier of a Josephson junction change the phase drop, ϕ, along the junction. The change in phase drop can be calculated by integrating (1.13) around the closed path shown in Fig.1.3 a). If the integration path lies far inside the superconductors where $\mathbf{J_s} = 0$ then the change in phase drop is

$$\phi(y_1) - \phi(y_2) = -\frac{2\pi\Phi}{\Phi_\circ} \tag{1.15}$$

where Φ is the flux through the loop. Since the magnetic field is confined to the junction area, the flux in the loop is simply the flux in the junction between y_1 and y_2. The junction

has a magnetic thickness $d = t + 2\lambda$ where λ is the penetration depth and t is the intrinsic width of the barrier material. If the local field in the junction is assumed uniform then $\mathbf{B} = B\hat{z}$ and the flux $\Phi = Bd(y_1 - y_2)$ so that

$$\phi(y_1) - \phi(y_2) = -\frac{2\pi Bd(y_1 - y_2)}{\Phi_\circ} \tag{1.16}$$

The critical current for the junction is found by integrating (1.11) over the entire junction. It can be shown that the critical current for a rectangular junction where $f(\phi) = sin(\phi)$ is

$$I = I_c \left| \frac{\sin(\pi\Phi/\Phi_\circ)}{\pi\Phi/\Phi_\circ} \right| \tag{1.17}$$

where I_c is the junction critical current in the absence of any magnetic field. This is the same Fraunhofer function in optics governing the intensity of light on a screen originating from a single slit diffraction grating. The analogy is completed by recognizing that $Bd(y_1 - y_2)/\Phi_\circ$ is equivalent to $sin(\theta)/\lambda$ where λ is the wavelength of light and θ is the angle, with respect to the screen normal, of the path of light illuminating a point on the screen. The Fraunhofer pattern is plotted in Fig.1.3 b) with the magnetic flux normalized to the flux quantum, $\Phi_\circ$. The largest peak occurs for zero applied field and the critical current is cancelled out for integer multiples of $\Phi_\circ$. The dependence of the critical current on the applied magnetic field is referred to as the junction's diffraction pattern.

Self Field Effects

The idealized diffraction pattern described by (1.17) applies only when magnetic fields due to currents in the junction can be neglected. This is the case for small junctions with small critical current densities. Screening of the external magnetic field in larger junctions induces asymmetries in the diffraction patterns with respect to magnetic field. The Josephson penetration depth, analogous to the bulk-material penetration depth, is a measure of the length scale of this screening.

$$\lambda_J = \sqrt{\frac{\hbar}{2e\mu_\circ J_c d}} \tag{1.18}$$

Here J_c is taken to be constant over the area of the junction and d is the magnetic thickness. Junctions with width $w < \lambda_J$ are in the short junction limit and will not have self field

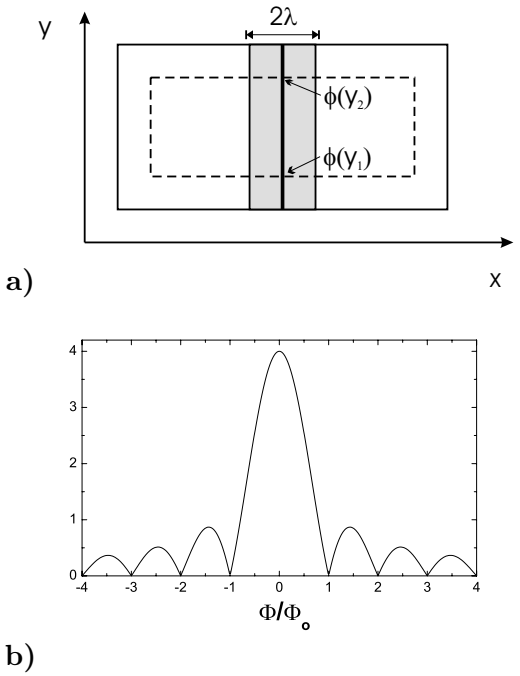

Figure 1.3: Magnetic fields in the junction change the phase drop along the junction. The dotted line indicates the integration path used to find the change along the junction. The barrier area is shaded to indicate the magnetic thickness.

effects. Junctions with $w > \lambda_J$ are in the long junction limit and will, in general, have asymmetric diffraction patterns.[3]

When J_c is not constant over the junction area the Josephson penetration depth is not well defined. In these cases it is difficult to classify junctions within a particular limit. Often, the junction characteristics must be measured to search for effects of self fields. This problem will be discussed in Chapter 3 in regard to grain boundary Josephson junctions.

1.3.2 Superconducting Quantum Interference Devices (SQUIDs)

Some useful devices can be fabricated by incorporating Josephson junctions into superconducting loops. The dependence of the phase on the magnetic field indicated above makes these devices extremely sensitive to magnetic fields. Two such devices are the *rf* SQUID, which incorporates a single junction into a loop, and the *dc* SQUID, containing two junctions in a single loop. More complicated devices can be fabricated with multiply-connected loops containing many junctions. Some of these devices may be useful to realize a solid-state

qubit for quantum computation.

rf SQUID

Recall from the derivation of (1.8) that the supercurrent density $\mathbf{J_s} = 0$ well inside the superconductor allowing (1.2) to be rewritten

$$-\Delta\theta = \frac{2e}{\hbar}\mathbf{A} \tag{1.19}$$

The phase is again calculated by integrating around the loop as shown in Fig. 2.4 a) but an additional phase term is added between points a and b due to the Josephson junction defined in (1.13). Performing the line integral around the loop the $-\Delta\theta$ term must be a multiple of 2π and the vector potential term yields the flux through the loop.

$$2\pi n = \left(\frac{2e}{\hbar}\right)\Phi + \phi \tag{1.20}$$

or

$$\phi = -2\pi\frac{\Phi}{\Phi_\circ} \tag{1.21}$$

These two equations show that the magnetic flux is no longer quantized but rather is proportional to the gauge invariant phase drop across the junction. The current in the loop is then

$$I = -I_c \sin\left(\frac{2\pi\Phi}{\Phi_\circ}\right) \tag{1.22}$$

The dependence of the circulating current on the flux is what makes this useful as a magnetometer. This SQUID is utilized by coupling an *rf* current into the loop with a tank circuit. The voltage across the tank circuit is dependent on the *rf* losses in the SQUID loop which can be shown to depend periodically on the static flux in the loop. The derivation of the *rf* SQUID response and control is complicated and will not be discussed here. This example is included to show that the sum of the phase contributions around the loop is quantized. The phase constraint, (1.20), can be applied to any superconducting loop containing an arbitrary number of junctions.[3; 14]

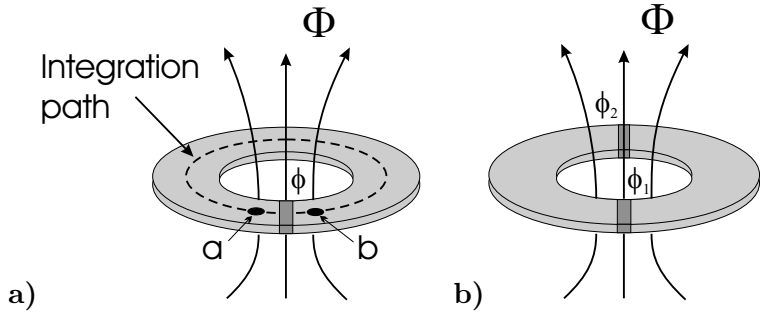

Figure 1.4: a) An *rf* SQUID loop. The junction adds an extra phase ϕ into the integral around the loop. b) A *dc* SQUID loop with two junction. These devices are useful as sensitive magnetometers, volt-meters, and current-meters.

dc SQUID

The superconducting ring forming a *dc* SQUID contains two junctions. Therefore, the flux in the loop can be related to the phase drops across the two junctions by

$$\phi_1 - \phi_2 = 2\pi \frac{\Phi}{\Phi_\circ} \tag{1.23}$$

where $\phi_{1,2}$ is the phase drop across the respective junction as shown in Fig. 2.4 b). If the two junctions are equal in size and barrier strength, the total current through the device is $I = I_c(sin\phi_1 + sin\phi_2)$. Using (1.23) to eliminate one of the phase variables and maximizing the resulting equation, it can be shown that the total current through the SQUID is related to the flux by

$$I_{SQ} = 2I_c \left| \cos \frac{\pi \Phi}{\Phi_\circ} \right| \tag{1.24}$$

The critical current of the SQUID is zero whenever the flux in the loop $\Phi = n\Phi_\circ/2$. This is analogous to the intensity of light originating from a distant Young's double slit diffraction grating where $\Phi/\Phi_\circ$ is equivalent to $l\, sin(\theta)/\lambda$. Here l is the distance between the two slits and θ is again the angle, with respect to the screen normal, of the path of light illuminating a point on the screen.

The *dc* SQUID is very useful for measuring small changes in magnetic field. However, the critical current dependance on the magnetic flux in (1.24) implies the SQUID would only be useful for measuring flux changes on the order of fractions of $\Phi_\circ$. It is typical to run the *dc* SQUID in a phase-locked-loop to give the device a larger dynamic range. In

this arrangement a feedback coil coupled to the SQUID loop maintains a constant flux in the loop cancelling out changes in the flux due to external magnetic fields. The feedback current needed to maintain the constant flux is proportional to the external flux.[3; 14]

Large Inductance Loops

If the inductance of the loop, L, is large the flux will have a term $\Phi_{cir} = LI_{cir}$ due to the circulating current in the loop. In this case the total flux becomes

$$\Phi = \Phi_{ex} + \Phi_{cir} = \Phi_{ex} + LI_{cir} \tag{1.25}$$

where I_{cir} is the circulating current in the loop. The circulating current in the *rf* SQUID is given by (1.22) so the external flux can be related to the total flux in the loop.

$$\Phi_{ex} = \Phi + LI_c \sin\left(2\pi\frac{\Phi}{\Phi_\circ}\right) \tag{1.26}$$

This equation can be inverted to show how Φ varies with external field Φ_{ex}. It is useful here to define a parameter

$$\beta_L = 2\pi\frac{LI_{cir}}{\Phi_\circ} \tag{1.27}$$

This is a measure of the importance of self-inductance in the loop. If this parameter is large ($\beta_L > 1$) then Φ's dependance on Φ_{ex} in (1.26) will be hysteretic. Hysteresis is required for the readout of a rf SQUID but too large a β_L requires strong coupling to the tank circuit. In the dc SQUID the circulating current is given by $(I_c/2)(\sin\phi_1 - \sin\phi_2)$ so the external flux is

$$\Phi_{ex} = \Phi + \frac{LI_c}{2}(\sin\phi_1 - \sin\phi_2) \tag{1.28}$$

In the limit of small current through the dc SQUID (1.28) can be written in the form

$$\Phi_{ex} = \Phi + LI_c \sin\left(\pi\frac{\Phi}{\Phi_\circ}\right) \tag{1.29}$$

and has a similar hysteretic dependence on the loop inductance as (1.26). In the dc SQUID a small inductance, $\beta_L \approx 1$, is needed to avoid hysteresis. If the inductance is too small the SQUID loses field sensitivity. It is extremely important to consider the effects of self inductance when designing superconducting circuits.

Chapter 2

Unconventional Superconductors

2.1 The Cuprate Materials

The cuprate superconductors are a class of ceramics in which some members exhibit transition temperatures (T_c) well above the boiling point of liquid nitrogen. Their carrier number density is significantly lower than low-temperature superconductors and their normal state resistivity is higher. All of the cuprates have a stacked perovskite-like structure containing CuO_2 planes separated by metal-oxide blocks. It is believed that superconductivity in these materials is two-dimensional occurring in the CuO_2 planes resulting in large discrepancies between in-plane and out-of-plane measurements of electrical properties. The properties of these materials can change drastically with both ion doping and oxygen concentration resulting in large families of compounds, differing in composition, whose members all exhibiting superconductivity. The material descriptions given here will be limited to the two materials used in this study, $YBa_2Cu_3O_{7-\delta}$ and $Bi_2Sr_2CaCu_2O_8$. A summary of the superconducting material properties is given in Table 2.1 showing the large anisotropy between in-plane and c-axis directions.

2.1.1 $\mathbf{YBa_2Cu_3O_{7-\delta}}$(YBCO)

YBCO has an orthorhombic room temperature phase with cell parameters a = 3.828Å, b = 3.888Å, and c = 11.65Å. The unit cell for YBCO is shown in Fig. 2.1 a). The

	$YBa_2Cu_3O_{7-\delta}$	$Bi_2Sr_2CaCu_2O_8$
λ_{ab}(Å)	1000-1400	3100
λ_c(Å)	5000-8000	-
ξ_{ab}(Å)	16-24	27-38
ξ_c(Å)	3-7	0.45-1.8

Table 2.1: The in-plane and out of plane properties of YBCO and BSCCO taken from refs. [15; 16] and references within.

c-axis length is three times the a&b-axes indicating the structure contains three stacked perovskite-like blocks. This material contains two CuO_2 planes in the center of the cell separated by a Y atom. This phase is observed at low temperatures $T \leq 500$K with oxygen content $0.0 \leq \delta \leq 0.6$. Outside these ranges, YBCO exhibits a tetragonal structure.[15]

The carrier concentration in the planes for this hole-doped material is controlled by the oxygen doping in the $Cu-O$ chains located at the ends of the unit cell. $T_c = 92$K for YBCO at optimal doping ($\delta = 0.16$) and decreases as δ increases. Superconductivity disappears at $\delta \cong 0.6$ coinciding with the transition to a tetragonal structure. The oxygen in the $Cu-O$ chains is highly mobile when the material is heated requiring care during material processing to avoid oxygen depletion.[15]

Transition metal cation substitutions, such as Ni and Zn, for in plane Cu has been shown to rapidly decrease transition temperatures and will destroy superconductivity at high concentrations. These magnetic impurities, substituted directly into the superconducting planes, interfere with the electron pairing dramatically effecting the superconducting properties. Other cations, such as Co and Al, substituted for Cu in the chains have lesser effects on the transition temperature. Total substitution of either of these elements in the chains does not destroy the superconductivity.[17] In general, the properties of the superconductor can be altered by partial replacement of Y or in-chain Cu with cations of different valency.[18]

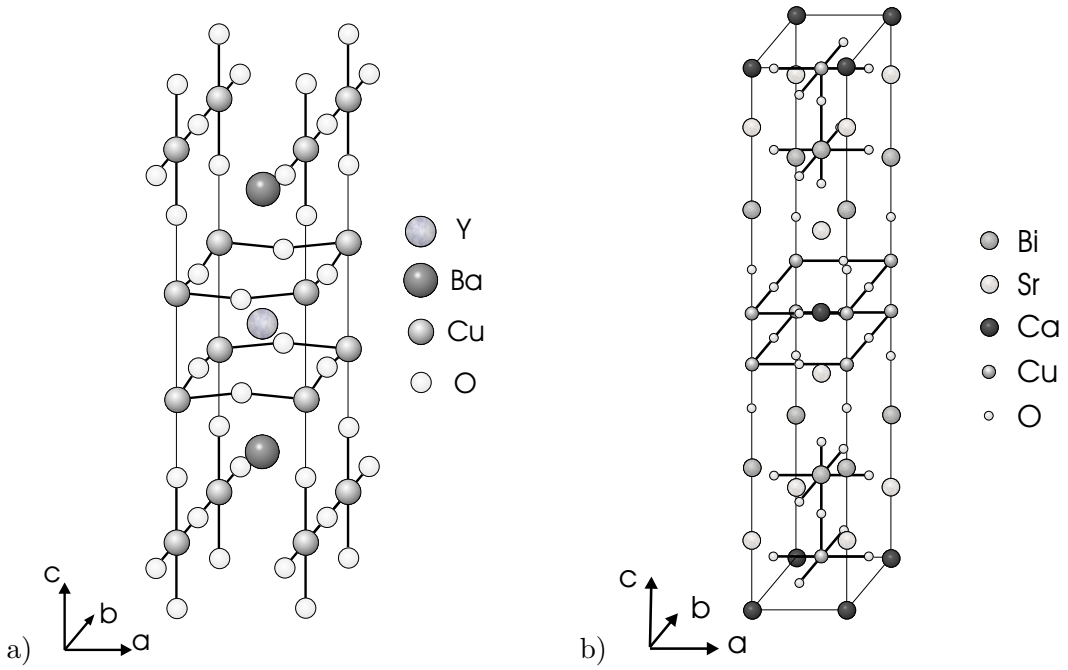

Figure 2.1: Crystal structure of a) orthorhombic $YBa_2Cu_3O_{7-\delta}$ and b) $Bi_2Sr_2CaCu_2O_8$. (These structures were reconstructed with information from refs. [15; 17; 19])

2.1.2 $Bi_2Sr_2CaCu_2O_8$(BSCCO)

BSCCO has an orthorhomic cell structure with cell parameters $a = 5.411$Å, $b = 5.418$Å,and $c = 30.89$Å. The BSCCO unit cell is shown in Fig. 2.1 b). The c-axis length is approximately 6 times larger than the a&b-axes again indicating multiple stacked perovskite-like blocks. This structure contains two CuO_2 planes separated by a Ca atom. These planes are flanked by SrO and BiO layers similar to the BaO layers in YBCO.[17]

This material belongs to an interesting family containing three phases $Bi_2Sr_2Ca_{n-1}Cu_nO_{2n+1}$ for $n = 1, 2, 3$(n also indicates the number of CuO_2 planes per unit cell). The $n = 3$ phase was the first material with a $T_c > 100$K and shows how T_c increases for larger numbers of CuO_2 planes. At optimal doping, the $n = 2$ phase of BSCCO has a maximum $T_c = 85$K. The carrier concentration in the planes are hole-like and are controlled by oxygen doping similar to YBCO. This material is also easily deoxygenated at high temperatures.

2.2 Determination of the Order Parameter Symmetry

Soon after the discovery of the high temperature cuprates[20] it was clear that the pairing mechanism could not be phonon mediated as described in the BCS theory. Flux quantization and Shapiro step experiments confirmed that the charge carriers were paired electrons, $e^* = 2e$, but the complex crystal structure precluded a three dimensional isotropic pairing symmetry.[15; 21] Experiments such as ARPES and Raman scattering, which were sensitive to the magnitude of the order parameter, Δ, indicated an anisotropic in-plane energy gap. Furthermore, measurement of the low temperature penetration depth, λ, indicated line nodes in the order parameter. A large number of symmetries based on different models were proposed to explain these results (some of the symmetries are plotted in Fig.1.2).[1] Several of these symmetries possessed anisotropic gaps such as anisotropic s-wave, $d_{x^2-y^2}$, as well as both complex and real admixtures of different symmetries. It became clear that a phase sensitive measurement was needed to distinguish between the competing symmetries. Experiments based on Josephson tunnelling were proposed to measure the phase along different crystal directions.

It is now well accepted that the cuprates have a dominant $d_{x^2-y^2}$ symmetry in the a-b plane as shown by many experiments. Three simple but very conclusive experiments are outlined below. The three experiments are the corner Josephson junction, the corner SQUID, and the tricrystal ring experiment. All three of these measurements indicate a π phase shift between orthogonal crystal directions consistent with a $d_{x^2-y^2}$ pairing symmetry. The first two experiments involve single crystal YBCO while the third experiment utilizes thin films and has been performed on several cuprates of both hole and electron doping.

2.2.1 Corner Josephson Junction Experiment

In this experiment a continuous junction is fabricated on two faces of a cuprate crystal with a conventional superconductor. The properties of each half of the junction depend on the

[1] There are several thorough reviews of these experiments and proposed order parameter symmetries. See refs.[7–9; 21; 22]

details of the order parameter perpendicular to the barrier. A schematic of this junction is shown in Fig. 2.2 a) & c) indicating the orientation of the s-wave and d-wave symmetries in real space. The total current through the junction can be found by integrating (1.11) over the length of the junction. If there is an additional phase shift due to the order parameter symmetry between the two crystal faces the integral must be performed on each face seperately. For an additional phase shift δ, due to the order parameter symmetry, integration of (1.11) yields the total current through the junction.

$$I = \frac{I_c}{\frac{\pi\Phi}{\Phi_\circ}} \left[\sin\left(\phi(0) + \frac{\delta}{2}\right) \left(\sin\left(\frac{\delta}{2}\right) + \sin\left(\frac{\pi\Phi}{\Phi_\circ} - \frac{\delta}{2}\right)\right)\right] \tag{2.1}$$

Here the two halves of the junction are assumed to be geometrically identical, $\phi(0)$ is the phase drop at the center of the junction relative to which all other phase drops are measured, and Φ is the total flux in the junction. For an isotropic s-wave order parameter there is no phase drop ($\delta = 0$) and (2.1) when maximized, reduces to (1.17). For $d_{x^2-y^2}$ or d_{xy} symmetries there is a π phase shift between orthogonal directions. When $\delta = \pi$, the total current in the junction (when maximized) becomes

$$I = I_c \left| \frac{\sin^2\left(\frac{\pi\Phi}{\Phi_\circ}\right)}{\frac{\pi\Phi}{\Phi_\circ}} \right| \tag{2.2}$$

The current is plotted in Fig. 2.2 d) as a function of applied flux. The Fraunhofer diffraction pattern from (1.17) is plotted in Fig. 2.2 b) for comparison. The diffraction pattern expected for a d-wave order parameter has zero critical current at zero field in stark contrast to the Fraunhofer pattern. For phase shifts other than π, the critical current zero would occur between 0 and $\Phi_\circ$ and would be asymmetric. In addition to the shifted location of the minima, the pattern has a modulation length of $2\Phi_\circ$.

The corner junction experiment was performed by Wollman et al.[22; 23] on single crystal YBCO with Au/Pb junctions. Figure 2.3 contains the diffractions patterns for two different corner junctions were the two crystal faces are perpendicular to the a and b axis. Both diffraction patterns show minima at zero applied field consistent with a $\delta = \pi$ phase shift. However, the critical current does not go to zero as found in (2.2). The authors

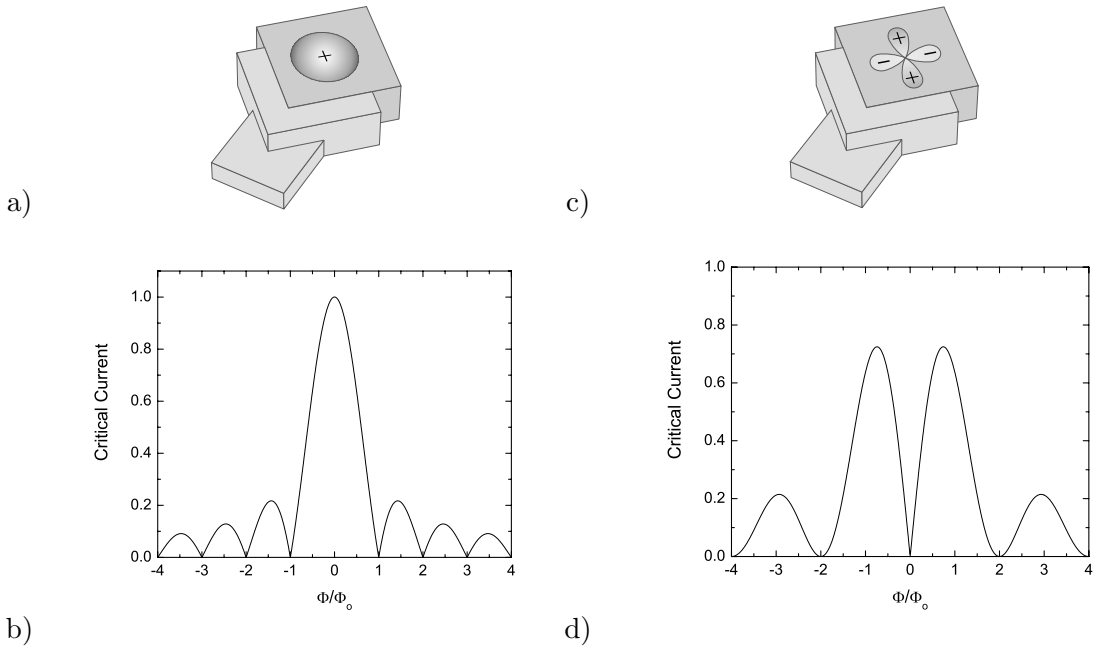

Figure 2.2: a)The corner junction experiment for a conventional superconductor produces the usual Fraunhofer diffraction pattern shown in c). For the d-wave case b) the π phase shift between the two halves of the junction shifts the diffraction pattern resulting in zero critical current for no applied magnetic field d).

are able to model the incomplete cancellation of current by assuming the two halves of the junction are not identical in size. The dashed line in Fig. 2.3 b) shows a calculated diffraction pattern for asymmetric junction halves. The occurrence of the critical current minima at zero applied field is the signature of a π phase shift.

2.2.2 Corner SQUID Experiment

The corner SQUID incorporates two Josephson junctions on faces of a cuprate single crystal with surface normals perpendicular to the a and b axis as shown in Fig. 2.4 a). The cuprate material comprises half of the SQUID and a conventional s-wave superconductor closes the loop. This configuration is also sensitive to any additional phase shift δ between the a and b axis due to the order parameter of the cuprate crystal. Summing the phases around the loop (1.23) yields

$$\phi_1 - \phi_2 + \delta = 2\pi \frac{\Phi}{\Phi_\circ} \tag{2.3}$$

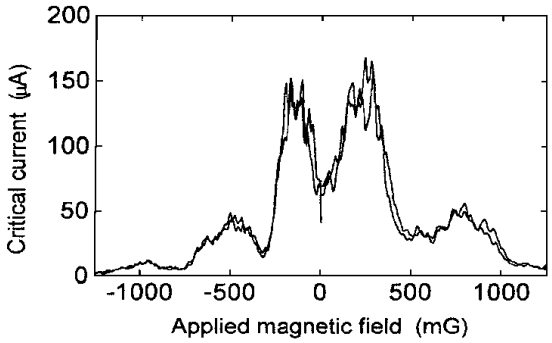

a)

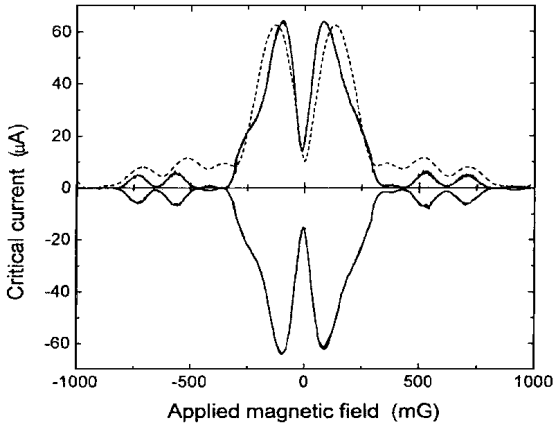

b)

Figure 2.3: Measured critical current as a function of applied magnetic field for two Josephson junctions straddeling the a and b faces of a YBCO crystal. The dashes line in b) is the calculated diffraction pattern assuming $d_{x^2-y^2}$ pairing and a 15% asymmetry in junction areas on the two faces. Figures taken from ref. [23]

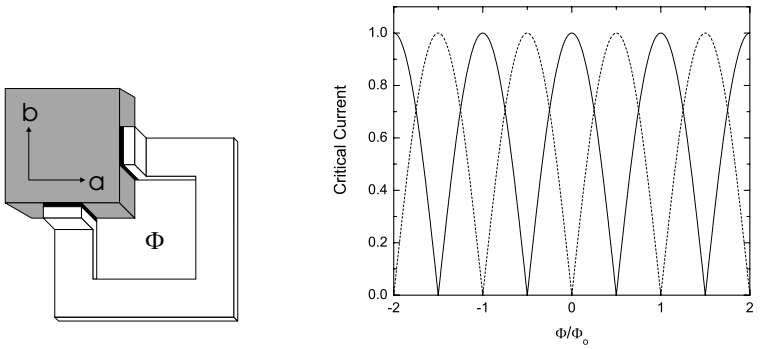

Figure 2.4: The corner SQUID uses two Josephson junctions to probe orthogonal directions in k-space. b) the current is plotted as a function of flux through the SQUID loop for s-wave(solid) and d-wave(dash) cases.

where $\Phi = \Phi_{ex} + LI_{cir}$ includes the self induced flux. In the limit of small inductance, the current through the SQUID is (from(1.24))

$$I_{SQ} = 2I_c \left| \cos\left(\pi \frac{\Phi}{\Phi_\circ} + \frac{\delta}{2}\right) \right| \tag{2.4}$$

Figure 2.4 b) has the current through the junction plotted as a function of external field for isotropic pairing (solid) and d-wave pairing (dashed) in the cuprate material. For $d_{x^2-y^2}$, $\delta = \pi$ and the pattern shifts such that the critical current at zero applied field is zero. This is analogous to the shift in diffraction pattern seen in the corner junction experiment. For a phase shift other than π the minimum would occur between 0 and $\Phi_\circ/2$ and the pattern would be asymmetric about zero magnetic field. If the loop inductance is significant ($\beta_L > 1$) the solution (2.4) is no longer valid. For non-negligible inductance the modulation of the critical current with applied flux will be reduced such that the critical current is never completely cancelled.

This experiment was also performed by Wollman et al.[22; 24] on a YBCO single crystal with Au/Pb films forming the junctions and SQUID loop. The authors reported difficulty obtaining good diffraction patterns for the SQUIDs due to critical current modulation of only a few percent, probably due to large inductances. To resolve this issue the dynamic resistance of the SQUID was measured as a function of the applied magnetic field. This is done by current biasing the SQUID near the critical current ($I \approx I_c$) and adding an

ac modulation to measure the dynamic resistance with a lock-in amplifier. Changes in the critical current will necessarily change the dynamic resistance such that a lowering of the critical current will raise the resistance. Natural asymmetries in the junctions and loop halves further complicate the interpretation of the data. When the current splits in the SQUID loop asymmetries introduce additional flux. This effect is observed by measuring the dynamic resistance for several different bias currents. The positions of maxima and minima can then be found by extrapolating to zero bias current. Figure 2.5 a) shows the dynamic resistance as a function of applied field for a corner SQUID at several bias currents. The markers indicate the first minima in the dynamic resistance for positive field. A minima in the resistance corresponds to a maxima in the critical current. This critical current maxima (resistance minima) moves closer to $0.5\Phi_\circ$ with decreasing bias current. Figure 2.5 b) shows the positions of critical current maxima as a function of SQUID bias current for a corner SQUID and an edge SQUID along with linear fits to the data. These data are for the same two SQUIDs cooled down several times. The linear fits to critical current maxima from the corner SQUID seem to converge at $0.5\Phi_\circ$ consistent with a π phase shift in the order parameter. The linear fits to critical current maxima from the edge SQUID are also plotted. This SQUID should not have any intrinsic phase shift because both junctions probe the same crystal direction. Linear fits of these critical current maxima extrapolate to zero, consistent with no intrinsic phase difference in the material.

2.2.3 Tricrystal Ring Experiment

The tricrystal ring experiment is an elegant way to measure for $d_{x^2-y^2}$ pairing symmetry using cuprate thin films. This technique utilizes grain boundary Josephson junctions that form naturally in cuprate thin films grown across a substrate grain boundary. The characteristics of these types of junctions will be discussed in detail in Section 3.1. For this experiment it is sufficient to know that a cuprate thin film grows with the orientation of the underlying substrate. The orientation mismatch at the grain boundary interface naturally forms a superconducting weak link.

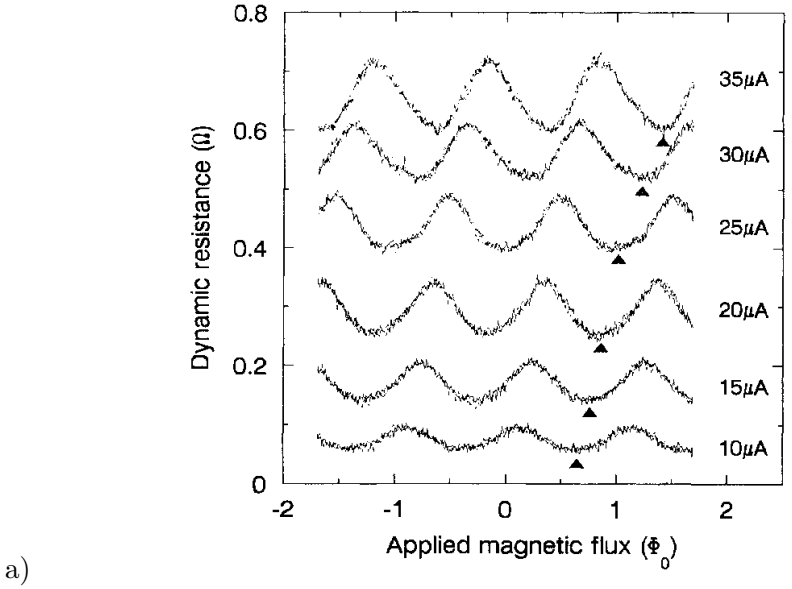

a)

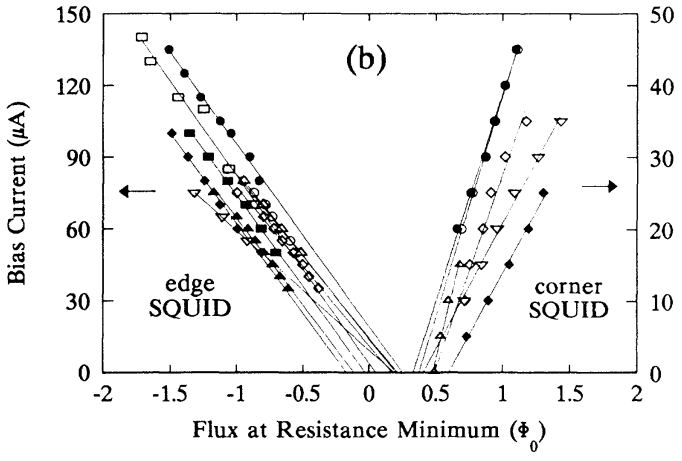

b)

Figure 2.5: a)Modulation of the dynamic resistance as a function of applied field for several bias currents. The markers indicate the position the first resistance minimum (critical current maximum) to the right of zero. b)Linear fits to resistance minima vs applied field for several edge SQUIDs and corner SQUIDs. The minima for the corner SQUIDs extrapolate to $0.5\Phi_\circ$, indicating a π phase shift, while minima for the edge SQUIDs extrapolate to 0. Figures taken from ref. [24]

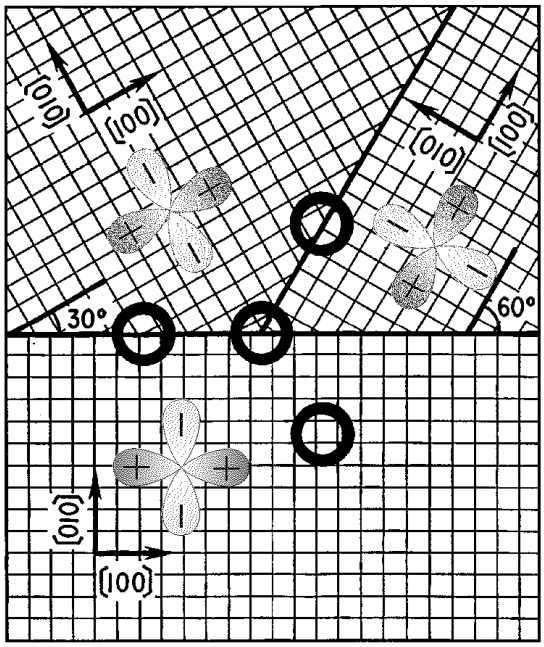

Figure 2.6: A diagram of the $SrTiO_3$ tricrystal used in the tricrystal ring experiment. d-wave cloverleafs have been added to show the orientation in each of the three crystal sections.

The substrate used in this experiment is a tricrystal specially constructed to have particular orientations of the grain boundaries and orientations between adjacent crystals. Figure 2.6 shows the construction of the tricrystal where the grid indicates the substrate orientation and the axis in each section denote the orientation of the cuprate thin film. (d-wave cloverleafs have been added as a guide to the eye.) The tricrystal ring is indicated in the figure as the central ring encircling the intersection point of all three grain boundaries. The other rings comprise a test group for the experiment. The two top sections of the substrate crystal have 30° and 60° orientations relative to the lower crystal. The grain boundary separating the top crystals is oriented at an angle of 60° relative to the horizontal grain boundary. In this particular orientation a ring encircling the grain boundary intersection point contains three junctions separating the three sections of cuprate film with different orientations. The junctions of the lower and upper left ring segments both sample the same lobe of the order parameter. Even though the two junctions for the upper left ring segment are 60° apart there is no intrinsic phase shift. The junctions of the upper right ring segment

have a relative phase shift of π (for d-wave symmetry). The phases in the ring can be added up in a similar fashion to the corner SQUID ring.

$$\phi_1 + \phi_2 + \phi_3 + \delta = \frac{2\pi\Phi}{\Phi_\circ} \tag{2.5}$$

The phases ϕ_j correspond to the phase drops across the three junctions and δ is again the phase shift intrinsic to the material. The total flux $\Phi = \Phi_{ex} + LI_{cir}$ for a loop of inductance L. The circulating current in the loop is related to the phase drops by the Josephson relation $I_{cir} = I_{c1}\sin(\phi_1) = I_{c2}\sin(\phi_2) = I_{c3}\sin(\phi_3)$. The circulating current is calculated using (2.5) assuming $\Phi_{ex} = 0$.

$$I_{cir} = \frac{\Phi_\circ}{2\pi L}(\phi_1 + \phi_2 + \phi_3 + \delta) \tag{2.6}$$

In the limit of large inductance, $LI_{cir} \gg \Phi_\circ$, the current through the ring will be small and $\phi_{1,2,3} \approx 0$. For d-wave symmetry $\delta = \pi$ and the loop spontaneously generates a circulating current such that $I_{cir}L \approx \Phi_\circ/2$.

This experiment was first proposed by Manfred Sigrist and T. M. Rice[25] to explain a paramagnetic effect seen experimentally in cuprate superconductors. It was first adapted as a phase sensitive test by Tsuei et al.[26] who fabricated rings of $YBa_2Cu_3O_{7-\delta}$ on a tricrystal with the geometry described above. The sample was cooled multiple times in zero magnetic field and a scanning SQUID microscope (SSM) was used to image the spontaneous flux generated in the loop. They were able to model the SSM response sufficiently well to measure a half flux quantum in the loop. This same group also performed this experiment on $Tl_2Ba_2CuO_{6+\delta}$[27], $Bi_2Sr_2CaCu_2O_8$[28], and in the two electron-doped cuprate materials $Pr_{1.85}Ce_{0.15}CuO_{4-y}$ and $Nd_{1.85}Ce_{0.15}CuO_{4-y}$, all showing evidence for a intrinsic π phase shift consistent with d-wave pairing. These results show that all tetragonal (or near tetragonal) cuprate materials probably have the same dominant d-wave pairing mechanism. [29] This same experiment has also been carried out on a YBCO corner-SQUID. The π phase shift intrinsic to the material generated a spontaneous current creating a flux in the SQUID loop $\Phi = 0.5\Phi_\circ$ which was imaged with an SSM.[30]

Terminology The literature regarding this experiment and others describes the ring encircling the GB intersection point as containing two 0-junctions and one π-junction. This is misleading because it implies the extra π phase drop occurs across a junction such that the phase $\phi_j = \pi$. Rather, the extra phase is intrinsic to a section of the ring whose junctions probe different lobes of the order parameter as explained above. The term π-junction should be reserved for a junction whose minimum Josephson energy occurs for a π phase drop across the junction.

2.3 Scattering Effects and Fragility of the $d_{x^2-y^2}$ Symmetry

2.3.1 Zero-Energy Bound States

An important result of d-wave pairing is the formation of surface-bound states at the Fermi energy. These so called zero-energy bound states (ZEBS) were first predicted by Hu[31] who suggested their existence as a phase sensitive test for d-wave pairing in the cuprates. Hu examined the case of a superconducting/normal metal (S/N) interface along the (110) (perpendicular to the node) direction. Quasiparticle Andreev reflections off the N/S interface form the bound states and sense the π phase shift of the d-wave order parameter. The bound state energies are found by solving the Bogoliubov-deGennes equations at the interface. These are modified Schrödinger equations for quasiparticles excitations in superconductors. The bound states energies for the N/S interface can be understood in terms of the phase constraint on the quasiparticle wave function forming the bound state. Following the notation in Bagwell[32], the total phase from all contributions must be 2π periodic.

$$2\cos^{-1}\left(\frac{E}{\Delta}\right) + \left(\frac{LE}{\xi_\circ \Delta}\right) \pm \phi = 2\pi n \tag{2.7}$$

Here L is the thickness of the normal metal layer, $\xi_\circ$ is the coherence length, Δ is the magnitude of the superconducting gap, and E is the bound-state energy. The first term on the left represents the phase due to the evanescent quasiparticle wave function in the superconductor. The second term is the phase from free electron and hole propagation in the normal metal. And, ϕ is the intrinsic phase drop picked up from the Andreev reflections.

For a (110) surface in the d-wave material, $L = 0$, $\phi = \pi$, and (2.7) yields bound-state energies at the Fermi energy($E = 0$).

The ZEBS at (110) interfaces are a direct result of the π phase shift intrinsic in the d-wave order parameter. A phase shift $\phi \neq \pi$ would move these states off zero energy. These bound states add to the density of states at the expense of the superconducting electrons, suppressing the order parameter, and should form in the vicinity of any scattering site such as impurities, surfaces, and interfaces. It has been suggested that a secondary pairing interaction masked in the bulk or nucleated at the scattering site could for a mixed symmetry. Buchholtz et al.[33] examined the effects of the d-wave pairing in the presence of an interface with an insulator using a quasiclassical formulation of superconductivity. The authors, assuming the superconductivity to be 2-dimensional with bulk d-wave pairing, consider real mixtures of several pairing symmetries allowed for tetragonal crystals such as $d_{x^2-y^2} + d_{xy}$. They show that for specular reflection from interfaces perpendicular to the nodes, the dominant d-wave pairing symmetry is suppressed at the interface and recovers within 6 coherence lengths. Further, the authors calculate that a real addition of a d_{xy} component is energetically favorable and could reduce the suppression of the mixed order parameter at the interface. The mixed pairing would have the result of rotating the d-wave cloverleaf such that a lobe is perpendicular to the interface.

Matsumoto and Shiba[34] consider a similar system but they do not constrain the relative phase of the order parameter mixture to 0 or π allowing for complex admixtures that break time-reversal symmetry. Their numerical calculations, where the initial phase between the two pairing symmetries in the complex plane is arbitrary, give complex solutions of the type $d_{x^2-y^2} \pm is$ and $d_{x^2-y^2} \pm id_{xy}$ where the relative phase converges to $\pm\pi/2$. These states would be energetically favorable due to removal of the nodes in the bulk d-wave symmetry resulting in a fully gapped order parameter. The magnitude and relative phase for these two complex functions are plotted in Fig. 1.2.

2.3.2 Broken Time-Reversal Symmetry

Time-reversal is performed classically by reversing the sign of t wherever it appears in equations governing the state of the system. For example, classical motion will obey Newton's laws with time running either forward or in reverse. Any system obeying Newton's laws is said to possess time-reversal symmetry (TRS). Time-reversal is performed in quantum mechanics by taking the complex conjugate of the wavefunction. Thus if the state of the system, Ψ, is complex then $\Psi \neq \Psi^*$ and the system breaks TRS. This can be generalized by saying TRS is broken when the system chooses a preferred orientation.[35]

Two systems already discussed that break TRS are the corner SQUID and the tricrystal ring experiment. When these two devices are cooled below T_c the loops spontaneously generates a half flux quantum. But the system must choose either clockwise or counterclockwise circulating currents and thus break TRS. In this example the symmetry is broken by the entire superconducting loop system. This is in contrast to a complex order parameter symmetry that intrinsically breaks TRS.

Mechanism of the $\mathbf{d \rightarrow d + is}$ Transition

The mechanism of formation of a complex surface state has been examined by Šimon Kos by using a Hubbard-Stratonovich transformation to write the total free energy in terms of single particle states. Using this formalism to consider s-wave pairing, the author shows that for an arbitrarily weak attraction, $|V_s|$, the system will favor a $d + is$ state. Only an imaginary s-wave component will effect the energy of the surface ZEBS creating states both above and below the Fermi energy. At $T = 0$ only the states below the Fermi energy will be filled lowering the energy of the system. This transition is thus driven by occupation of the ZEBS at a surface or interface. The author also calculates the spatial extent of the complex s-wave component showing it decays into the bulk as ξ/x^2 for $x > \xi$ where x is the distance from the interface.[36–38] Thus the ZEBS created by the bulk d-wave pairing symmetry at a (110) interface make the system unstable to a $d + is$ transition. The complex component exists near the interface and creates a fully formed gap.

The fragility of the d-wave order parameter in the presence of scattering sites is due to the intrinsic π phase shift forming ZEBS. These bound states should drive the transition to a complex order parameter leading to novel superconducting phases with broken TRS. The effects of surfaces and interfaces are also important for utilizing cuprate materials in device fabrication. Zero-bias conductance peaks in quasiparticle tunnel junctions and the low-temperature anomaly in penetration depth measurements are strong evident for the existence of the ZEBS.[39]

Quasiparticle Tunneling

Electron tunnelling is an excellent probe of the quasiparticle density of states in a superconductor. This is the usual quantum-mechanical tunnelling that occurs between two conductors separated by a thin insulator. The insulator can be an insulating material as in thin film tunnel junctions or a vacuum as for STM tunnelling spectra. Derivation of the tunnelling spectra is simplified by use of the semiconductor model to calculate the tunneling currents. In this model the current is dependent on the voltage, V, applied to the tunnel junction and the density of states of the two conductors. For a superconducting material, the density of states has an energy gap, Δ, around the Fermi surface where the quasiparticle states are excluded. Figure 2.7 a) shows the semiconductor model description for an N-S tunnel junction. The applied voltage shifts the chemical potentials of the two conductors by an amount ev. All tunnelling processes are direct so at $T = 0$ there is no current until filled states from one conductor line up with empty states of the other. The current at a particular voltage is written

$$I = A|T|^2 \int_{-\infty}^{\infty} N_1(E)N_2(E+eV)[f(E) - f(E+eV)]dE \tag{2.8}$$

where $N_{1,2}(E)$ is the density of states of the normal metal and superconductor respectively and $f(E)$ is the Fermi function. The differential conductance is then given by

$$G_{ns}\Big|_{T=0} = \frac{dI_{ns}}{dV}\Big|_{T=0} = G_{nn}\frac{N_{2s}(e|V|)}{N_2(0)} \tag{2.9}$$

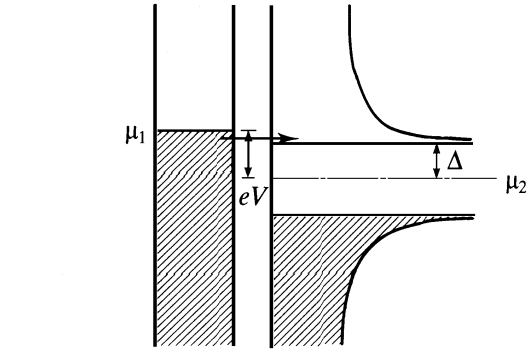

a)

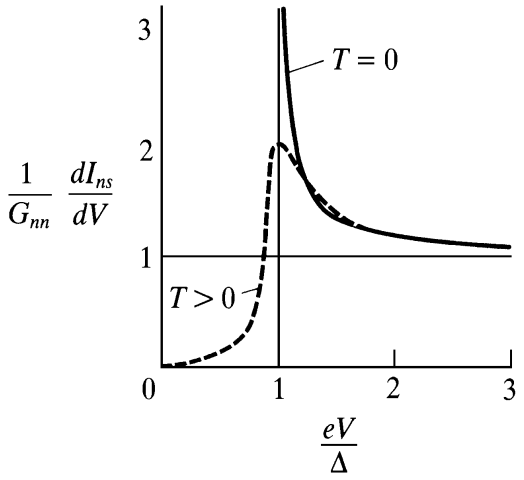

b)

Figure 2.7: a)The semiconductor model for tunnelling between a normal metal and a superconductor. b) The differential conductance maps out the density of states and measures the magnitude of the superconducting gap. This figure is taken from ref. [14] pages 73 & 76.

where G_{nn} and $N_2(0)$ are the differential conductance and the density of states of the superconductor in the normal state. For higher temperature, $T \neq 0$, the conductance is smeared by the Fermi function. Figure 2.7 b) shows the differential conductance from (2.9) for $T = 0$ (solid) and $T \neq 0$ (dash).

Tunnelling into cuprate superconductors produces vastly different differential conductance curves, due to the anisotropic order parameter, versus what is predicted for conventional superconductors.[40–44] Tunnelling spectra for YBCO show significant density of quasiparticle states below a gap-like feature (GLF) due to the low energy excitations

allowed in the nodes. The GLF is a measure of the maximum (lobe) energy gap. For tunnel directions parallel to the a-b plane in YBCO a peak in the conductance is observed at zero voltage. The magnitude of the zero-bias conductance peak is dependent on the tunneling direction relative to the crystal axes with a maximum conductance occurring for tunnelling into the nodes of the d-wave order parameter. This peak is believed to be a direct measurement of the bound states at zero energy predicted by Hu.[45; 46]

Some zero-bias conductance peaks observed in YBCO/I/Cu and YBCO/I/In tunnel junctions show splitting when the temperature is lowered below 8K and 6K respectively.[42; 43; 47] This splitting may be evidence for a broken TRS state due to the interaction of the bulk d-wave symmetry with the surface forming a complex order parameter.[46] Such a state would produce phase shifts other than 0 or π between different k-space directions producing bound surface-states with non-zero energies as calculated from (2.7). The shift of the conductance peaks to non-zero energies is consistent with the transition to a complex surface symmetry below some critical temperature.

2.3.3 Magnetic Impurities

Magnetic impurities can also provide scattering cites where the bulk d-wave order parameter may be suppressed. A theory put forth by Balatsky[48] predicts a suppression of the bulk order parameter around the magnetic impurities. He argues that a spin-orbit interaction generates complex d_{xy} pairing resulting in islands of $d_{x^2-y^2} + id_{xy}$ around the impurities over a length scale of the coherence length. Regions of complex order are not constrained to an interface or surface and occur throughout the material. At high concentrations of magnetic impurity atoms the islands of complex order should Josephson couple causing a bulk transition to $d_{x^2-y^2} + id_{xy}$.

This spin-orbit coupling model for magnetic impurities was developed as a plausible explanation for a drop in the thermal conductivity observed in single crystal BSCCO doped with Ni by Movshovich et al.[49] The thermal conductivity drops below a critical temperature $T^* \approx 200$mK to 80% below the pre-transition value. Above T^* the conductivity,

$\kappa \propto T^{\alpha}$ has power law behavior with $\alpha \approx 1.7$ while below the transition κ is linear in T. The authors calculate that the phonon contribution to the low temperature thermal conductivity is too small to account for the drop. They conclude the effect must be electronic in origin and speculate, from comparison of the drop to the superconducting transition in Al, that it is consistent with a fully gapped order parameter.

2.4 Conclusions

There is evidence that the d-wave order parameter that is dominant in the bulk is suppressed at interfaces perpendicular to the node directions. This suppression opens up the possibility of an alternate pairing mechanism that exists within a few coherence lengths of the surface. Observance of the zero bias conductance peaks and subsequent splitting of this peak is highly suggestive that the secondary pairing mechanism is out of phase with the bulk pairing creating a complex order parameter. A separate bulk transition to a complex $d_{x^2-y^2} + id_{xy}$ has been predicted at low temperatures for cuprates doped with magnetic impurities. A drop in thermal conductivity seen in Ni-doped BSCCO is consistent with such a transition.

Transition to a complex order parameter, either on the surface or in the bulk, would significantly change the properties of the superconductor. A well designed experiment that is sensitive to the phase of the order parameter should detect such a transition. To date, measurements performed to detect these transitions have been plagued by poor interface quality. For example, only recently have interfaces been formed allowing for angle resolved measurements of the zero-bias conductance peaks.[44] This thesis examines the use Josephson interferometry on grain boundary junctions to gain access to clean interfaces created in-situ for use in measurement sensitive to the transition to a complex order parameter.

Chapter 3

Grain Boundary Josephson Junctions

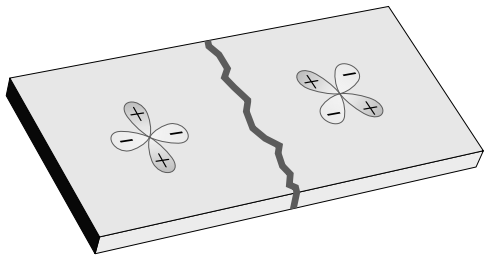

The short coherence lengths of the cuprate materials allow significant suppression of the order parameter in the presence of defects in the crystal. Introducing defects through engineered grain boundaries is a simple method for creating Josephson weak links in cuprate thin films. Grain boundaries are formed between different regions of material with different angles of orientation. There are several methods for creating oriented grains in the cuprates including bi-crystal grain boundaries, grown on a bicrystal substrate, bi-epitaxial grain boundaries, created by a seed layer that rotates the overlying film, and step edge grain boundaries, created by growing film on a substrate containing sharp steps.[50] The cuprate junctions studied in this thesis are [001]-tilt grain boundaries grown on $SrTiO_3$ bicrystals. Fabrication of the junctions is described in Chapter 4.

This chapter outlines the properties of these bi-crystal grain boundary interfaces and

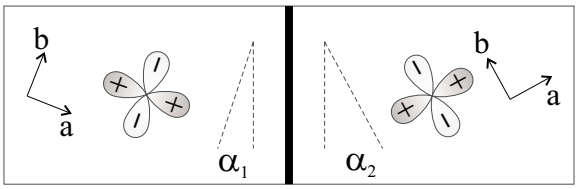

Figure 3.1: The geometry of the grain boundary is determined by the two angles, α_1 and α_2 with the overall angle $\theta = \alpha_1 + \alpha_2$. A junction is called symmetric if $\alpha_1 = -\alpha_2$ and asymmetric if $\alpha_1 = 0$ and $\alpha_2 = \theta$.

the characteristics of the Josephson junction created. A simple model based on the interface properties of these junctions is introduced to calculate the junction behavior for different order parameter symmetries. The results of these calculations are discussed and a signature for a transition to a complex symmetry is identified.

3.1 Bicrystal Grain Boundary Interfaces

Bi-crystal grain boundaries are created when a cuprate film is epitaxially grown on a suitable bicrystal substrate whose two crystal halves have some arbitrary relative orientation. The orientation of the overlying cuprate film is determined by the substrate crystal and the resulting grain boundary follows that of the substrate. The transport properties across the boundary are determined by the angle between the two grains. For small angles, $\theta < 10°$ for YBCO, the grains are strongly coupled and the critical current density is limited by vortex motion along the boundary. For larger angles, the grains Josephson couple, exhibiting weak-link behavior.[50–53] The critical current decreases exponentially with increasing angle to a minimum at $\theta = 45°$. This decrease is due to the anisotropic d-wave order parameter coupled with a faceted interface, dislocations, and band bending effects reducing the carrier density at the boundary.[54; 55] Figure 3.1 shows the orientation of two grains relative to the grain boundary for a bicrystal substrate. The overall angle between the grains is $\theta = \alpha_1 + \alpha_2$. In this study, a grain boundary is called symmetric when $\alpha_1 = \alpha_2$ and asymmetric when $\alpha_1 = 0$ and $\theta = \alpha_2$.

The current-voltage (IV) characteristics of the junctions exhibit overdamped behavior

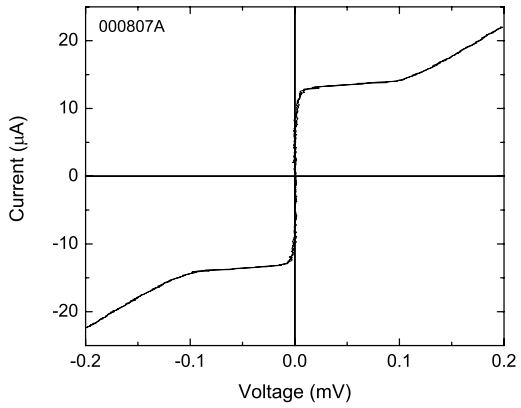

Figure 3.2: The IV curve for a $10\mu m$ junction on a 45° asymmetric $SrTiO_3$ bicrystal. The curve deviates from the RSJ model showing a kink in the normal state.

that can be approximated by the resistively-shunted junction model (RSJ) including effects of thermal activated phase slips.[50; 56; 57] In the RSJ model the current through the junction has a supercurrent component and a normal component

$$I = I_c \sin(\phi) + \frac{V}{R_n} \tag{3.1}$$

where R_n is the normal state resistance of the junction. The mean voltage across the junction, $V_\circ$, is then given by

$$\left(\frac{V_\circ}{R_n}\right)^2 = I^2 - I_c^2 \tag{3.2}$$

Phase slips are thermally activated with an energy barrier $\gamma = \hbar I_c(T)/ek_BT$. These phase slips persist well below the critical temperature in grain boundary junctions resulting in rounded IV curves. Figure 3.2 shows the IV curve for a 10μm, 45° asymmetric grain boundary junction measured at 1.6K with a critical current of 12μA. The curve is noise rounded and does not approach the normal state resistance value smoothly as predicted by the RSJ model. This is typical of the IV characteristics for all the junctions studied here.

3.1.1 Boundary Facets

The grain boundary created in the cuprate thin film grown on a bicrystal meanders and does not perfectly follow the substrate. The resulting interface is composed of many small

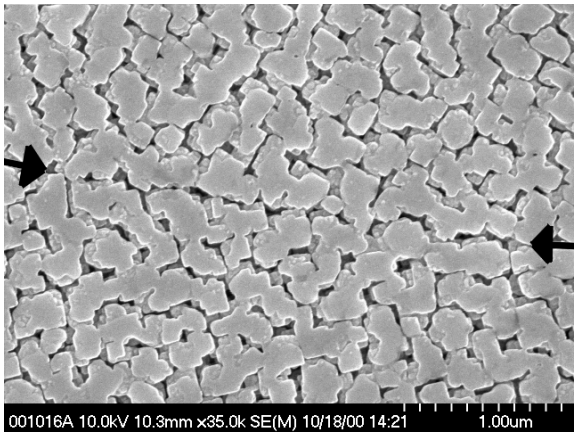

Figure 3.3: A SEM micrograph of 45° symmetric grain boundary in a laser ablated YBCO film. Arrows indicate the location of the boundary.

facets whose size is dependent on the film growth parameters. This meander occurs due to competition at the interface between growth islands of different orientation. Figure 3.3 is a SEM micrograph of a YBCO thin film grown on a 45° symmetric $SrTiO_3$ bicrystal. The individual growth islands are clearly visible with the arrows indicating the location of the grain boundary showing a meandering faceted structure. The scale in the lower right corner indicates the facets are $10 - 300$ nm in size, consistent with other laser ablated films.[58]

The optimal grain boundary orientation to probe the d-wave node direction, desired for this study, occurs for 45° asymmetric junctions ($\alpha_1 = 0$ and $\alpha_2 = 45°$ in Fig. 3.1). This geometry provides access to a clean (110) interface created *in-situ*. In this orientation, the facets have a dramatic effect on the transport properties across the grain boundary. The directional nature of the Josephson tunneling means adjacent facets with sufficiently large angle will tunnel into lobes of opposite sign as shown in Fig. 3.4 a). The π phase difference produces a critical current density of opposite sign causing a near complete cancellation of the junction critical current. The magnitude of the order parameter will also vary with facet direction affecting the magnitude of the critical current density for each facet. The resulting diffraction pattern is determined by the facet structure. Figure 3.4 b) shows the diffraction pattern for a 45° asymmetric YBCO junction taken at $6K$. The pattern shows a distinct departure from the usual Fraunhofer pattern predicted for a uniform barrier with a uniform critical current density. Figure 3.4 c) shows the diffraction pattern of a 24° symmetric

YBCO junction taken at $87K$ for comparison. In the 24° symmetric junction only a few large angle facets will tunnel into a lobe of opposite sign. There is less cancellation and the resulting diffraction pattern is reminiscent of the usual Fraunhofer pattern with the maximum critical current occurring at zero applied magnetic field. The deviations are due almost entirely to a non-uniform critical current density along the junction.[55; 58]

The details of the diffraction pattern for large angle grain boundary junctions are dependent on the facet structure in the boundary and are analogous to a fingerprint of the junction. The diffraction pattern for each junction will be unique but they share some common features. All of the diffraction patterns are symmetric about zero applied field in the absence of self-field effects. This is expected for any real order parameter symmetry. Also, the maximum critical current of the junction occurs at some non-zero magnetic field, in contrast to the Fraunhofer pattern. However, this magnetic field value will still be relatively close to zero field due to the overall drop in the critical current magnitude with increasing field. This decrease in the critical current is due to the magnetic phase winding along the barrier which causes a local cancellation of the critical current. The phase winding creates the characteristic decay of the critical current in the Fraunhofer diffraction pattern described by (1.17). A d-wave junction with a faceted barrier is subject to the same cancellation. Lastly, the width of the peaks is determined by the overall size of the junction independent of the facet size. The facet structure determines which peaks are suppressed or magnified.[55]

The Josephson Penetration Depth The non-uniform current density caused by the faceting makes it difficult to define the Josephson penetration depth, λ_J, for the grain boundary junctions. This fact is typically ignored and λ_J is calculated using a critical current density that is averaged over the junction. The junction whose IV curve is shown in Fig. 3.2 has an area $A = 3 \times 10^{-12}$ m^2 resulting in $J_c = 4 \times 10^6$A/m^2. Plugging this number into (1.18) with $d = 2\lambda = 2000$Å gives for the Josephson penetration depth $\lambda_J = 18\mu$m. While this calculation would indicate the 10μm junction is in the short junction limit, a

a)

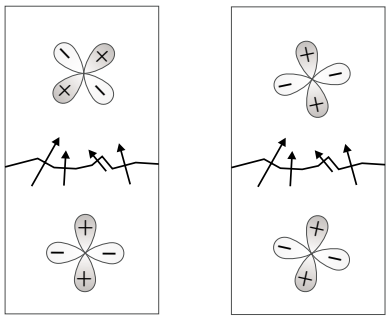

b)

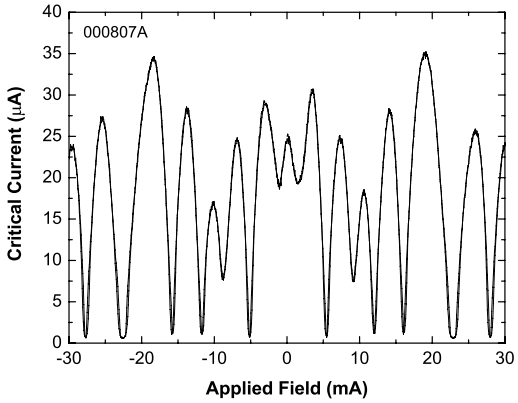

c)

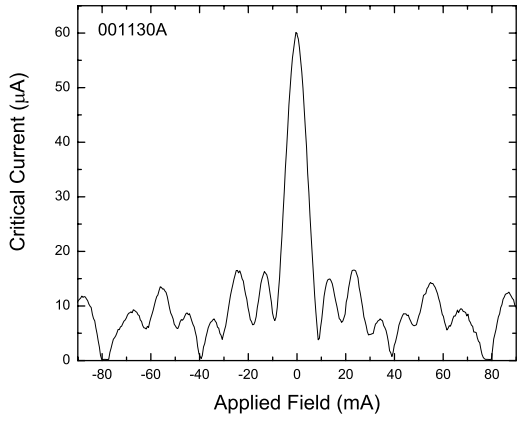

Figure 3.4: a)The directional Josephson tunneling probes different k-space directions on each facet effecting the transport properties across a grain boundary. b)The diffraction pattern for a $20\mu m$, 45° asymmetric junction at $6K$ shows anomalous field dependence while c) a $15\mu m$, 24° symmetric junction produces a diffraction pattern with features more similar to the Fraunhofer pattern.

single facet with a large critical current could introduce asymmetries into the diffraction pattern. This type of calculation is a good approximation but does not guarantee the absence of self-field effects. The diffraction pattern in Fig. 3.4 c) was measured at 87K to lower the critical current to obtain a symmetric pattern. This 24° symmetric junction has higher critical current densities resulting in a smaller average λ_J.

3.2 Junction Simulations

The characteristics of the grain boundary Josephson junction can be captured in a relatively simple theoretical model. Neglecting self-field effects, each facet can be treated as an independent junction with the junction parameters determined by the angle of the grain boundary and the relative angle of the facet. The total current is then only a sum of the currents of all the facets assuming phase coherence along the junction. This simple model was proposed by Copetti et al. to validate the use of grain boundary junctions as a test for d-wave symmetry.[59]

For a junction of width w whose grain boundary lies along the y axis, the current density, utilizing (1.11) with $f(\phi) = sin(\phi)$, is given by

$$J_c(y, B, T, \phi_\circ) = J_{c0}(y, T) sin\left(2\pi \frac{\Phi(y, B)}{\Phi_\circ} + \phi_{drop}(y, T) + \phi_\circ\right) \tag{3.3}$$

The facets influence the model through the y dependence of the critical current density, J_{c0}, and the local phase drop across the junction, ϕ_{drop}. (These factors will, in general, also be dependent on the temperature, T, and will be addressed below.) The phase at a point along the junction is dependent on the magnetic flux in the barrier, $\Phi(y, B)$, the intrinsic phase difference between the order parameter on either side of the grain boundary, ϕ_{drop}, and an arbitrary phase constant, $\phi_\circ$. This phase constant is a reference point relative to which all other phases are measured. For these calculations the reference is chosen as the phase at the center($y = 0$) of the junction. The critical current density is proportional to the product of the magnitudes of the left and right order parameters.

$$J_{c0}(y, T) = \Delta_l(y, T)\Delta_r(y, T) \tag{3.4}$$

This definition is sufficient to recover the properties of the grain boundary Josephson junction. The total current through the junction is then

$$I = \int_{-w/2}^{w/2} J_{c0}(y) sin(\phi(y)) dy \tag{3.5}$$

where ϕ is the phase due to all the contributions above. Once the integral is performed, the arbitrary phase factor, $\phi_\circ$ is varied to maximize the total current.

The effects of different order parameter symmetries enter into the model through the definitions of the magnitudes of the order parameters, $\Delta_{l,r}$ and the intrinsic phase drop, ϕ_{drop}. For an s-wave superconductor, the magnitude is isotropic and the intrinsic phase drop is zero regardless of facet angle. For a d-wave material, the magnitude varies and phase vary as a function of facet angle. The details of any particular order parameter can be plugged into this model to calculate the critical current through the junction for any applied field, B.

3.2.1 Diffraction Patterns

Magnetic diffraction patterns are calculated in this model by integrating (3.5) for each value of the applied magnetic field. The field is related to the phase through (1.16). Figure 3.5 a) shows a randomly generated grain boundary containing 30 facets. The corresponding diffraction patterns assuming s-wave (dashed) and d-wave (solid) symmetry are plotted in Fig. 3.5 for a 45° asymmetric junction geometry. The applied magnetic field is plotted as the total flux threading the junction, normalized to $\Phi_\circ$. As mentioned earlier and evident from the calculated diffraction patterns, it is the magnetic junction area that determines the period of oscillations. This modulation length of the diffraction pattern is independent of the facet size. The s-wave calculation returns the expected Fraunhofer diffraction pattern indicating the facets do not affect the transport properties of the junction. The diffraction pattern calculated for d-wave symmetry is significantly altered. This pattern is symmetric about zero applied field but is significantly reduced in magnitude from the s-wave case. The maximum critical current occurs at $\Phi \approx 6\Phi_\circ$. Lastly, the details of the calculated

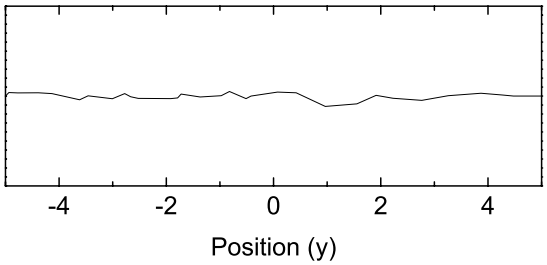

a)

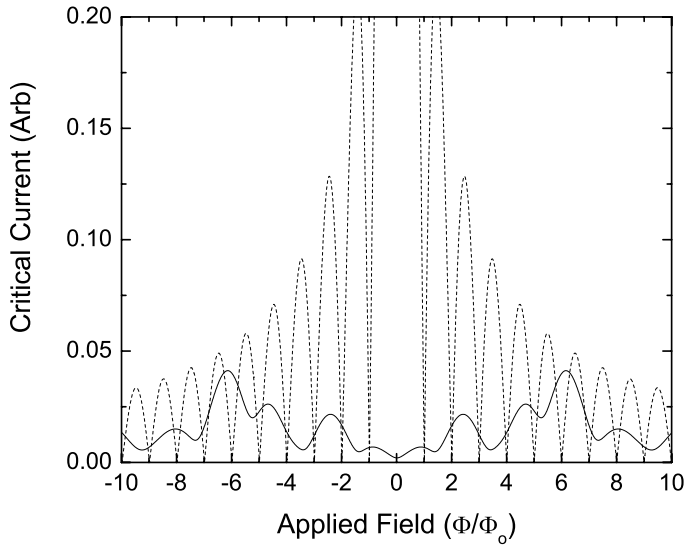

b)

Figure 3.5: a)A randomly generated grain boundary containing 30 facets. b)The simulated diffraction patterns for the artificial boundary in a 45° asymmetric junction geometry for s-wave (dashed) and d-wave (solid).

d-wave diffraction pattern show significant structure originating from the boundary facets. This simple model recreates the behavior observed in cuprate grain boundary Josephson junctions yielding a useful tool for predicting junction behavior through a transition of the pairing symmetry.

3.3 Signature of Complex Order Parameters

Calculations performed using complex order parameter symmetries depend on the symmetry and the relative strength of the secondary pairing. Figure 1.2 e) & f) show the magnitude

and phase of complex symmetries $d_{x^2-y^2} + i\epsilon s$ and $d_{x^2-y^2} + i\epsilon d_{xy}$ plotted as a function of k-space direction for $\epsilon = 0.2$. ϵ is the ratio of the maximum subdominant and dominant energy gaps, ($\epsilon = \Delta_{sub}/\Delta_{dom}$). The complex order parameters differ from the other order parameters in Fig. 1.2 in that they allow phase shifts other than 0 or π between different k-space directions. Figure 3.6 shows the simulated diffraction patterns for $d_{x^2-y^2} + i\epsilon s$ with $\epsilon = 0.0, 0.05, 0.1, 0.15, 0.2$. The complex order parameter introduces large asymmetries with respect to field into the diffraction pattern. There is also a dramatic rise in critical current at zero field. Both the asymmetry and the increase in critical current grow in magnitude with an increase in the subdominant component. The increase in the critical current occurs due to the loss of nodes in the order parameter. The dependence of the critical current density on the magnitude of the order parameter, defined in (3.4), combined with the 45° asymmetric junction geometry cause this dramatic increase, even for small values of ϵ. The asymmetry in the diffraction pattern is caused by intrinsic phase shifts across the facets of values other than 0 or π. A similar asymmetry would have been seen in the corner junction and SQUID experiments, described in Section 2.2, for a phase shift other than π. Calculated results for $d_{x^2-y^2} + i\epsilon d_{xy}$ are not shown but are nearly identical.

3.3.1 Temperature Dependence of the Critical Current

The splitting of the zero-bias conductance peak, thought to indicate a transition to a complex pairing symmetry at the surface, occurs when the tunnel junctions are cooled below $T \approx 15$K. Similarly, the transition to a bulk complex pairing symmetry due to magnetic impurities is predicted to occur as the material is cooled to low temperatures. The grain boundary junctions should therefore show an abrupt change in their transport properties below some transition temperature. The temperature dependence of the transition is easily added to the junction model by including a temperature dependence of the magnitude of the dominant and subdominant order parameters. To do this, a temperature dependence of the order parameter is used that approximates the order parameter temperature dependence

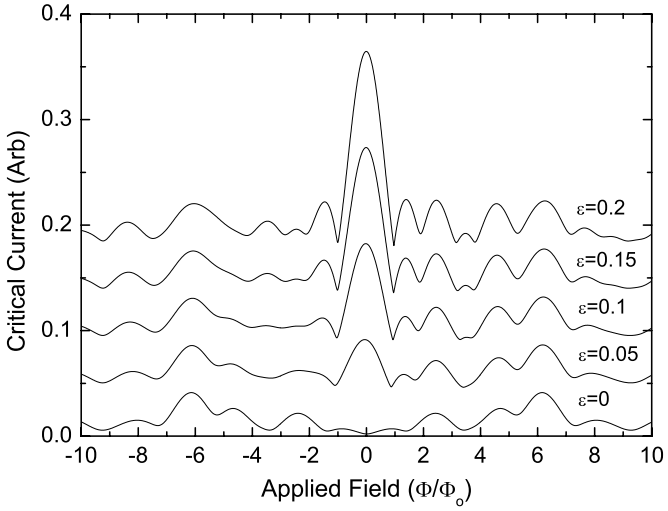

Figure 3.6: The simulated diffraction patterns for a 45° asymmetric junction assuming $d_{x^2-y^2} + i\epsilon s$ symmetry for $\epsilon = 0.0, 0.05, 0.1, 0.15, 0.2$. The critical current at zero field increases with increasing ϵ and the diffraction patterns become asymmetric.

calculated from BCS theory in the weak coupling limit.

$$\Delta = \Delta_\circ \left(1 - \left(\frac{T}{T_c}\right)^2\right) \tag{3.6}$$

This equation is multiplied by ϵ to give the temperature dependence of the subdominant order parameter whose critical temperature becomes $T^* = \epsilon T_c$.[1]

Figure 3.7 plots the critical current as a function of the temperature at zero applied field for the order parameter temperature dependence in (3.6). The critical current, assuming a pure d-wave order parameter (solid), shows a smooth increase with decreasing temperature. The critical current for a $d_{x^2-y^2} + i0.05s$ order parameter (dashed), where the subdominant critical temperature is $T^* = 0.05T_c$, shows a sharp increase for $T < T^*$. The effect of the temperature dependence in (3.6) is equivalent to changing ϵ and the increase in critical current with decreased temperature is consistent with the behavior in Fig. 3.6 for an increasing subdominant order parameter.

[1]This temperature dependence is used to show the general behavior of a junction undergoing a transition to a complex order parameter and is not meant as a rigorous calculation.

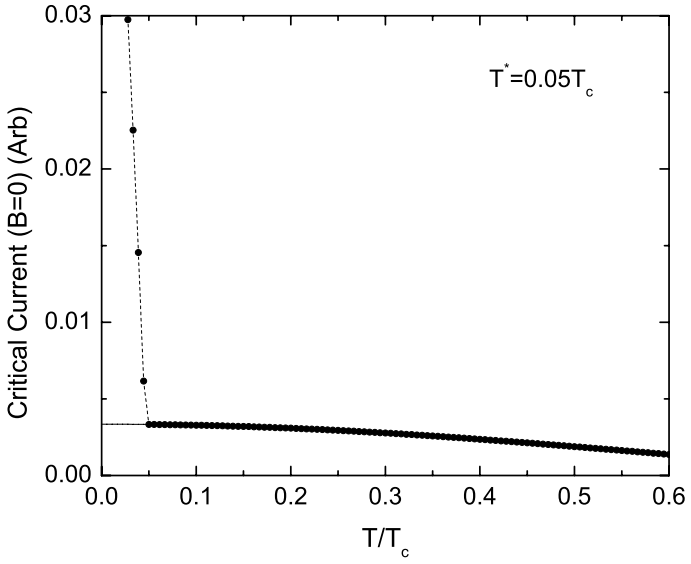

Figure 3.7: The critical current plotted as a function of temperature for pure d-wave (solid) and complex $d + i\epsilon s$ (dashed) order parameters.

3.3.2 Experimental Test

The onset of a complex pairing symmetry of either $d_{x^2-y^2} + i\epsilon s$ or $d_{x^2-y^2} + i\epsilon d_{xy}$ should dramatically change the characteristics of the diffraction pattern and the critical current as a function of temperature for a 45° asymmetric grain boundary Josephson junction. If this transition occurs at some temperature $0 < T^* < T_c$, moving the junction through this temperature should change the junction in a controllable and reversible way. The critical current at zero field should increase dramatically with a kink at T^*. Also, the asymmetry in the diffraction pattern below T^* should be a dramatic departure from the symmetric pattern above T^*. These changes should be reversible to show they do not occur due to trapped flux or stray fields.

3.3.3 Quantifying the Asymmetry

The human eye is exceptionally good at discerning asymmetries. Simple observation of the simulated diffraction patterns reveal large amounts of asymmetry even for complex order

parameters with a small fraction of subdominant pairing. Existing peaks shift in magnetic field location and change in magnitude while new peaks are created. While these qualitative changes in asymmetry are easy to observe, quantifying the asymmetry to compare simulations with measured results is more difficult. An asymmetry parameter, α, for the diffraction patterns can be defined as the sum of the magnitude of the critical current difference at each field point.

$$\alpha = \int_0^{B_\circ} \frac{2}{B_\circ} \left| \frac{I_c(B) - I_c(-B)}{I_c(B) + I_c(-B)} \right| dB \tag{3.7}$$

Here the critical current difference is normalized by the average critical current at each field value. This asymmetry parameter can be used to quantify the asymmetry in the calculated diffraction patterns. Each field point B_i has a corresponding negative field point reducing the integral in (3.7) to a sum. Figure 3.8 a) shows the asymmetry parameter, α, plotted as a function of the subdominant strength, ϵ, for four random facet sets. The sum is performed out to a field value of $300\Phi_\circ$. The asymmetry increases with increasing ϵ and the results for each facet set are qualitatively the same. In Fig. 3.8 b) the sum is only performed out to a field value of $10\Phi_\circ$ and the asymmetry becomes dependent on the different facet sets. There is a large rise in asymmetry at small ϵ and two of the facet sets show decreases in the asymmetry above $\epsilon = 0.35$. This indicates that a majority of the asymmetry occurs near zero field, not over the entire diffraction pattern. And, the region where the asymmetry occurs is pushed out to higher fields with increasing ϵ causing the drop in α for two of the facet sets.

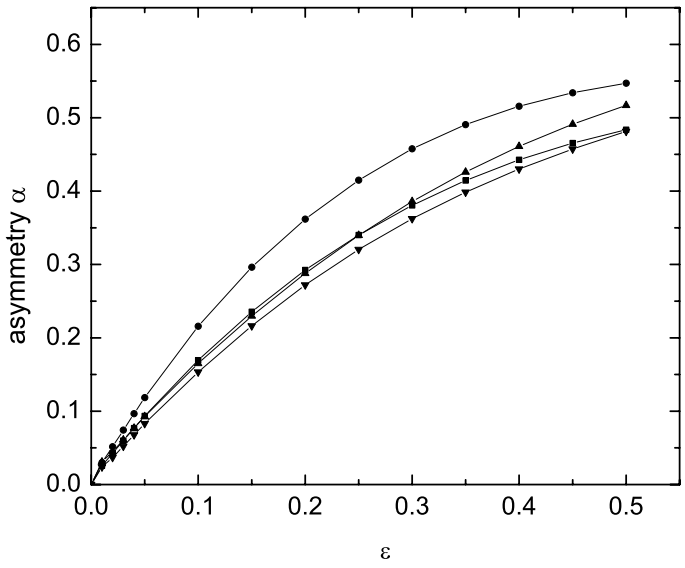

a)

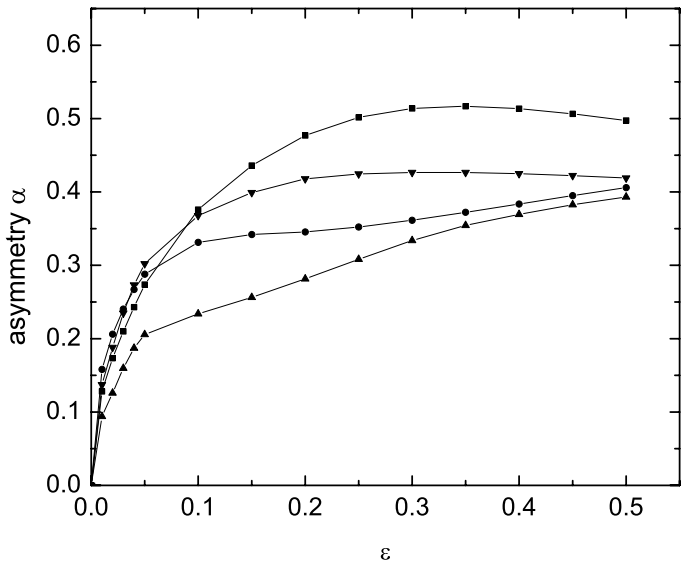

b)

Figure 3.8: Asymmetry plotted as a function of the strength of the subdominant pairing for $d_{x^2-y^2} + i\epsilon s$ for four sets of facets. For, a) asymmetry summed out to $300\Phi_\circ$ and, b) asymmetry summed out to $10\Phi_\circ$.

Chapter 4

Fabrication and Measurement Techniques

The devices fabricated and measured in this study were all high-temperature cuprate grain boundary junctions formed on bicrystal substrates. The two cuprate materials studied were $YBa_2Cu_3O_{7-\delta}$ and $Bi_2Sr_2CaCu_2O_8$. This chapter describes the methods used to fabricate these thin film materials, both with and without dopants, and the photolithographic processing used to define the devices. The films were cooled and measured in a ^3He insert and a dilution refrigerator to reach mK temperatures. Both these cryogenic methods are discussed in detail.

4.1 Thin Film Fabrication

The materials of interest in this study are high-T_c cuprate films with and without impurity dopants. In all the growth processes optimal oxygen doping, as measured by the critical temperature, was the target. Table A.1 on page 92 lists the known characteristics of each film used in this study along with the stoichiometry and the junction geometry.

Material	*Crystal Structure*	*Unit Cell Spacing*		
		a(Å)	b(Å)	c(Å)
$SrTiO_3$(substrate)	cubic	3.905	3.905	3.905
$YBa_2Cu_3O_{7-\delta}$ [16]	orthorhombic	3.8227	3.8872	11.6802
$Bi_2Sr_2CaCu_2O_8$ [16]	orthorhombic	5.411	5.418	30.89

Table 4.1: The unit cell spacing for YBCO and BSCCO showing why $SrTiO_3$ substrates are used.

4.1.1 Substrates

All thin films used in this study were fabricated on commercially available $SrTiO_3$ bi-crystal substrates. The $SrTiO_3$ bi-crystals are formed by fusing two single crystals together in the desired orientation forming a grain boundary. The fused crystals are then cut and polished to a $1cm \times 1cm \times 0.5mm$ size such that the grain boundary runs through the center of the substrate, parallel to one side. The orientation of the bi-crystal can be checked by x-ray diffraction analysis. Crystal orientation is usually found to be within 1° of the desired orientation for commercially produced substrates.

$SrTiO_3$ substrates are ideal for growing many cuprate materials due to the unit cell size being well matched. This ensures that the thin films will grow epitaxially with the underlying orientation of the substrate. A grain boundary will form in the thin film due to the mismatched orientation at the bi-crystal grain boundary. Table 4.1 shows the unit cell spacing of $SrTiO_3$ along with the cell spacing of YBCO and BSCCO. The bi-crystal substrates are very expensive and are reused when possible. Old patterned films are removed and the substrate surface is polished with a silica suspension using a Buehler Minimet polisher. This technique provides reproducible film results.

4.1.2 Laser Ablation

Laser Ablation is a thin film deposition technique that utilizes a high energy laser pulse to vaporize a stoichiometric target material. This allows for thin films of complex compounds

containing many elements to be fabricated with accurate control of the film stoichiometry. The deposition occurs in a vacuum chamber often in an atmosphere of a particular process gas at pressures below 1 torr. The plume of vaporized target material is directed at a substrate that can be heated. The process gas and substrate material recipe is determined by the type of material being grown. This deposition technique produces high quality YBCO films.[60]

The Ablation Chamber

The $YBa_2Cu_3O_{7-\delta}$ along with the Ni-doped $YBa_2Cu_3O_{7-\delta}$ thin films were grown in a custom built laser ablation system utilizing a Lambda Physik Compex 301 laser running an ArF gas mixture ($\lambda = 198nm$). The bi-crystal substrates were mounted with silver paint onto a movable heater stage capable of reaching temperatures of 850C. Typical target to substrate distance was 5-6cm. Use of a mass flow controller and an iris valve on the turbo pump allowed for accurate control of O_2 pressure and flow in the vacuum chamber. A quartz lenz was used to focus the laser pulse onto the target resulting in a spot size roughly 6×2mm resulting in a energy density $\approx 0.6\text{J}/cm^2$. The Ni doped $YBa_2Cu_3O_{7-\delta}$ films were grown in a smaller chamber with equivalent capabilities to the chamber described above. The smaller chamber was used to prevent magnetic contamination of the main growth chamber.

$\mathbf{YBa_2Cu_3O_{7-\delta}}$ Growth Procedure

The substrates were heated prior to ablation to allow the substrate and silver paint to outgas. Once a base pressure of 5×10^{-7}torr was reached with the substrate at the target deposition temperature T_d, O_2 was added to anneal the substrate and clean the surface. The ablation was performed at a target O_2 pressure, P_d, while the substrate was scanned relative to the plume to ensure a uniform film over the entire substrate. A typical ablation lasted 5 minutes running the laser at 3Hz resulting in a film thickness around 2000Å. After ablation, the temperature was lowered and the film annealed in an O_2 atmosphere for a time t_{an} to achieve optimal doping. Typical parameters for the growth process and anneal

Material	$T_d(C)$	$P_d(mtorr)$	$T_{an}(C)$	$t_{an}(min)$
$YBa_2Cu_3O_{7-\delta}$	780	500	450	60
$YBa_2Cu_{2.91}Ni_{0.09}O_{7-\delta}$	800	250	425	60
$YBa_2Cu_{2.85}Ni_{0.15}O_{7-\delta}$	800	250	425	60
$Y_{0.7}Ca_{0.3}Ba_2Cu_3O_{7-\delta}$	760	190	–	slowly cooled
$YBa_2Cu_{2.9}Co_{0.1}O_{7-\delta}$	760	190	–	slowly cooled

Table 4.2: Laser ablation parameters used form $YBa_2Cu_3O_{7-\delta}$ and Ni, Ca, Co-doped $YBa_2Cu_3O_{7-\delta}$.

are given in Table 4.2.

Ca and Co Doping One Ca and one Co doped $YBa_2Cu_3O_{7-\delta}$ film were obtained from J. Mannhart's research group at the Institute of Physics in Augsburg, Germany. Both films were laser ablated on $SrTiO_3$ bi-crystals with 45° asymmetric geometries. The typical growth parameters for these films listed in Table 4.2 are taken from ref [61].

4.1.3 Off-Axis Sputtering

Sputtering is a physical vapor deposition technique involving the removal of target material by ionized particles accelerated toward the target. For single element metals sputtered with a non-reactive gas, sputtering processes are easily described by elastic collision cascades caused by the impact of the incident particles. When a multicomponent target is used the process is far more complicated with different elements sputtering at different rates unrelated to their concentration in the target material and often involves a reactive gas plasma. Off-axis sputtering refers to situations when the sample is positioned somewhere other than directly in front of the target. Extensive research has been done to understand these processes and determine useful recipes for different compounds.[62]

It was discovered shortly after the discovery of $YBa_2Cu_3O_{7-\delta}$ that off-axis sputtering produced high quality films with good transition temperatures.[63; 64] The substrate is commonly held at an angle of 90° relative to the surface of the target off to one side. A

mixture of O_2 and Ar process gas is used for optimal doping. The substrate angle minimizes oxygen re-sputtering at the sample and produces stoichiometric films but deposition rates are extremely low. Recent studies have confirmed that the 90° geometry is optimal for growing c-axis $YBa_2Cu_3O_{7-\delta}$ with clean surfaces.[65]

The Pr-doped YBCO films used in this study were grown by Xiaoqing Yu in an off-axis growth chamber maintained by Laura Greene at the University of Illinois. An on-stoichiometric target was used in an atmosphere of (4:1) Ar:O_2 at a pressure of 170mTorr. The substrate was positioned in the off-axis geometry detailed above and heated to a temperature of $735°C$.

4.1.4 Molecular Beam Epitaxy

Atomic Layer-by-Layer Molecular Beam Epitaxy (ALL-MBE) involves sequential deposition of atoms to control the evolution of the chemical reaction on a crystalline surface. This is achieved by accurately controlling the flux of atoms at the substrate within 1% and monitoring the film surface structure. The ALL-MBE system uses Knudson cell thermal evaporation sources to provide stable atomic beam fluxes over many hours. The flux from each source is accurately measured by atomic absorption spectroscopy and the cell shutters are computer controlled to allow for accurate growth of complex multi-layered structures.[66]

The film surface structure is monitored in situ by Reflection High-Energy Electron Diffraction (RHEED) on an atomic scale. A thin electron beam with energy 10KeV and a low angle of incidence diffracts the surface probing the periodicity. The electron diffraction produces a k-space representation of the surface structure when monitored in the far field yielding in situ real-time details of the growth.

The $Bi_2Sr_2CaCu_2O_8$ films used in this study were grown by Seong-shik Oh in a ALL-MBE growth system maintained by James Eckstein at the University of Illinois.

4.1.5 Contact Layer

To obtain low resistance contact to the cuprate films it is desirable to deposit a noble metal capping layer. Early samples measured in this study used conducting silver paint electrical contacts where the leads were glued to the sample. These contacts were inconsistent and unreliable when thermally cycled. The contact resistance on some leads made in this way would increase with decreasing temperature into the $M\Omega$ range rendering the lead useless. Later films used Au capping layers deposited *ex-situ* with a shadow-mask covering the grain boundary to prevent contamination. The contact resistance for capping layers deposited *ex-situ* are still high and require an anneal at high temperatures before low resistance is realized.[67] These oxygen anneals often resulted in degradation of the transition temperature and width resulting in an unknown oxygen doping after the anneal.

In-situ deposition of a capping layer in the grain boundary cuprate system requires either the removal of the noble metal from the grain boundary or masking the boundary during deposition. A wet etch for Au films using an aqueous solution of potassium iodide (KI) and iodide (I) has been used on some films. This etchant has been shown to give Au etch rates of $200-300$Å/min without etching YBCO or the substrate.[68] The aqueous solution, however, has been shown to damage the surface of both YBCO and BSCCO.[69; 70] Later YBCO samples used this etch to remove the *in-situ* deposited Au layer but this method is not preferred if accurate knowledge of the junction critical current density is sought. The Au top layer on the BSCCO sample 1795 was deposited *in-situ* with a shadow mask protecting the grain boundary.

4.1.6 Film Characterization

Film quality was tested by measuring the room temperature sheet resistance and the superconducting transition temperature. When possible, the sheet resistance was measured immediately after the film was grown and removed from vacuum. Films with low sheet resistance ($\approx 800\Omega$) were ideal. Transition temperatures for the YBCO films grown in Urbana were measured by *ac* susceptibility in a flow-through cold-finger cryostat. Susceptibility was

measured using a standard two-coil opposite-side technique with a lock-in amplifier. A four terminal resistivity measurement was performed on the BSCCO films and Ca, Co-doped YBCO films to find the critical temperature.

Due to the wide range of fabrication techniques and dopants used in this study, the critical temperatures recorded as well as their transition width were varied. Table A.1 lists all the bicrystal geometries and the transition temperatures for the different films. The specific data for samples 990625A and 001103A are unavailable but the transition temperatures were consistent with other films of similar composition.

4.2 Device Definition

The Josephson junctions and chip wiring are defined by ion milling with a photoresist mask. Since the junctions are naturally present at the grain boundary and the contact layer is deposited prior to patterning, there is only one patterning step to define the devices. This makes well defined grain boundary Josephson junctions on bi-crystal substrates very easy to fabricate with reproducible results.

4.2.1 Photolithography

Photoresist (PR) is used as a milling mask to protect the junctions and wiring while excess material is removed. All photolithography was performed in the Microfabrication Facility of the Material Research Laboratory in the class 100 clean room. Masks were written by e-beam lithography by John Hughes in the Microelectronics Laboratory on Cr-quartz 4in masks. Often copies of the master mask were used to prevent damage to the original. The copies were created on FeO-on-glass blanks.

The first step of the process was to spin AZ5214 PR (both straight and thinned are used) onto the cuprate sample at 4000 RPM resulting in a resist layer about 1.8μm thick ($\approx$ 1.2μm when thinned). A 30sec bake on a 90°C hotplate was performed to remove solvents and harden the PR. The resist was then exposed to broad band UV light, created by a Hg vapor lamp, through the positive mask using a Karl Suss MJB3 aligner in contact mode. In this

mode, the mask is pressed up against the sample to allow for an accurate pattern transfer. Typical exposure times were 3.5sec at an intensity of 15.0mW/cm^2. The PR was developed in AZ351 developer and water (5:1 H_2O:AZ351) to remove the resist that was exposed to the UV light. AZ5214 is a positive resist so the mask pattern positive was reproduced on the sample protecting the cuprate material beneath.

4.2.2 Ion Milling

Excess film material was removed by bombarding the sample with Ar atoms using process called ion milling. All samples in this study were milled with a Commonwealth Scientific 8cm ion gun with a Commonwealth ID3501 power source in a vacuum system maintained by the Microfabrication Facility. The system was pumped out to a base pressure of 5×10^{-6}torr and Ar was injected to raise the pressure to 4×10^{-4}torr. Milling was performed at a beam voltage of 300V and beam currents of 80-100mA. To protect the cuprate film the sample was mounted on a LN_2 cooled stage located 30cm from the ion gun and cooled to -70°C during milling to prevent the ion gun from heating the sample, deoxygenating the film. The ion gun was run at a beam voltage of 350V and a beam current of 80-100mA resulting in typical mill times of approximately 10 minutes for 2000Å films. After milling the photoresist was removed with acetone in an ultrasound followed by an isopropanol rinse.

Figure 4.1 is a picture of a patterned and milled YBCO film showing strips running across the grain boundary forming the Josephson junctions. There are three mask patterns used in this study each with different junction sizes. Three patterns were necessary to measure junctions of different materials with vastly different critical current densities.

4.2.3 Film Damage

It is very important when patterning cuprate films to avoid heating and exposure to water. Heating can change the oxygen content of the films and degrade the T_c. Avoiding unnecessary heating steps and cooling the sample during ion milling helped to maintain film quality. In addition, the ion mill was run at beam voltages below 300V to reduce ex-

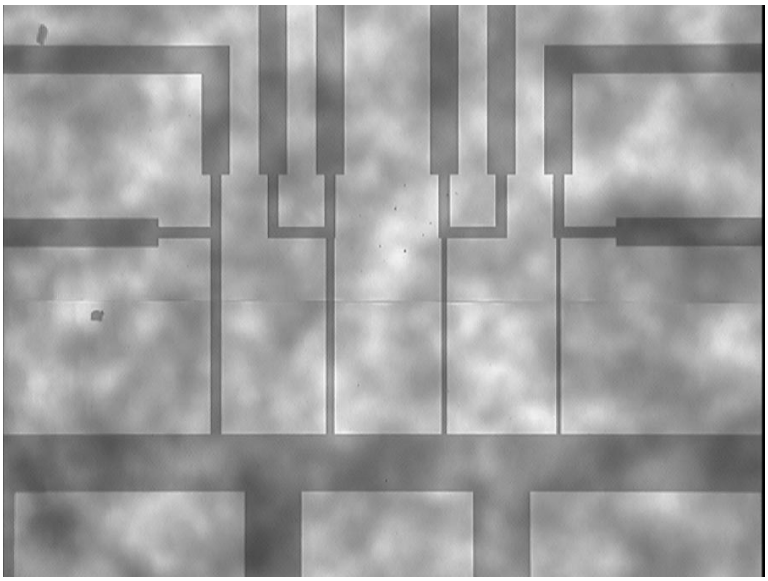

Figure 4.1: A picture of patterned $YBa_2Cu_3O_{7-\delta}$ Josephson junctions on a 45° asymmetric bi-crystal. The bi-crystal grain boundary is visible as a faint horizontal line. The junctions run vertically across the grain boundary and from right to left are nominally $20\mu m$, $15\mu m$, $10\mu m$, and $5\mu m$ wide.

cess surface heating of the sample. Relatively short exposure times to water would destroy superconductivity to a significant depth in cuprate films.[68–70] To reduce these damaging effects, great care was taken to align the sample correctly with the first exposure. This ensured that the remaining material, after ion milling, has had no exposure to the water based developer. In addition to these precautionary steps, a post developer bake at 130C, typical for AZ5214 photoresist processing, was omitted to prevent deoxygenation. All of these steps have been shown to greatly increase the reproducibility of the devices without significantly affecting the photolithographic quality.[71]

4.3 Junctions Measurements

4.3.1 Cryogenics

Measurement of the Josephson junction characteristics took place in a Heliox 2^{VL} ^3He Insert and a Kelvinox 25 Dilution Refrigerator, both manufactured by Oxford Instruments Ltd., resulting in access to stable temperature control from 100mK to 80K. The samples

were mounted on a custom built Cu stage/coil assembly incorporating heat-sunk resistive filters and a Hemholtz coil into one compact setup capable of being mounted on both inserts. Electrical connections were built into both inserts with standard plug connectors at the top and bottom of the insert. Both systems were run in super-insulated ^4He dewars with hold times in excess of 10 hours. Magnetic shielding was provide by μ-metal cans surrounding the dewars. The ^3He-insert also had a Pb shield maintained at 4.2K for additional magnetic shielding. This provided a quiet electrical and magnetic measurement environment.

Heliox2^{VL} ^{3}He Insert

The Heliox2^{VL} is a closed system ^3He insert with a base temperature of 350mK. The sample stage/coil assembly was mounted on the ^3He pot inside a vacuum can allowing the stage to be heated in excess of 80K with minimal LHe boil off. The four main components of the insert are: the ^3He reservoir, the ^3He pot, the sorption pump, and the 1K pot. Both the sorption pump and the 1K pot can draw He from the bath for cooling purposes. The 1K pot is attached to a pump to lower the temperature of the helium in the pot to $\approx$ 1.4K To reach base temperature, the sorption pump is heated above 40K to release the ^3He. The ^3He is then condensed by the 1K pot and collects into the ^3He pot. Once all of the ^3He is condensed, the sorption pump is cooled again lowering the vapor pressure in the ^3Hepot and reducing the temperature. This system is controlled with a Oxford ITC503 controller.[72]

Dilution Refrigerator

The Kelvinox 25 dilution refrigerator is an insert that operates from 1K down to 30mK (with no heat load; 100mk with the stage/coil assembly mounted). The cooling power is provided by the $^3He/^4He$ mixture separating into two phases, ^3He rich and ^4He rich, below a critical temperature allowing the ^3He to diffuses across the phase boundary. This phase separation occurs in the mixing chamber after the mixture is condensed through the 1K pot (similar to the operation of the ^3He insert). The ^4He rich phase is continuously pumped

and condensed back into the ^3He rich phase maintaining the concentration gradient across the phase boundary. The dilution refrigerator has a cooling power of 25μW at 100mK and can be run indefinitely as long as the ^4He reservoir is refilled periodically.[73; 74]

4.3.2 Electrical Measurements

Each junction can be characterized by measuring its IV curve and I_c as a function of applied magnetic field and temperature. An IV curve is measured with a low-noise preamplifier and a voltage controlled current source controlled by a data acquisition computer. The critical current is measured either with a voltage criterion or by an averaged differential resistance method. Figure 4.2 is a schematic of the electrical setup used to measure the critical current with a lock-in amplifier to measure the differential resistance. The *ac* reference signal from the lock-in and the *dc* error signal from the PID controller are summed and fed into the current source input. The custom built current source is battery powered for low noise and a low noise preamplifier is used to isolate the junction. The differential resistance measured in the lock-in is compared to the set point by the PID controller and an error signal is generated, completing the circuit. If a voltage criterion is used, the voltage signal from the preamplifier is fed directly into the PID controller bypassing the lock-in.

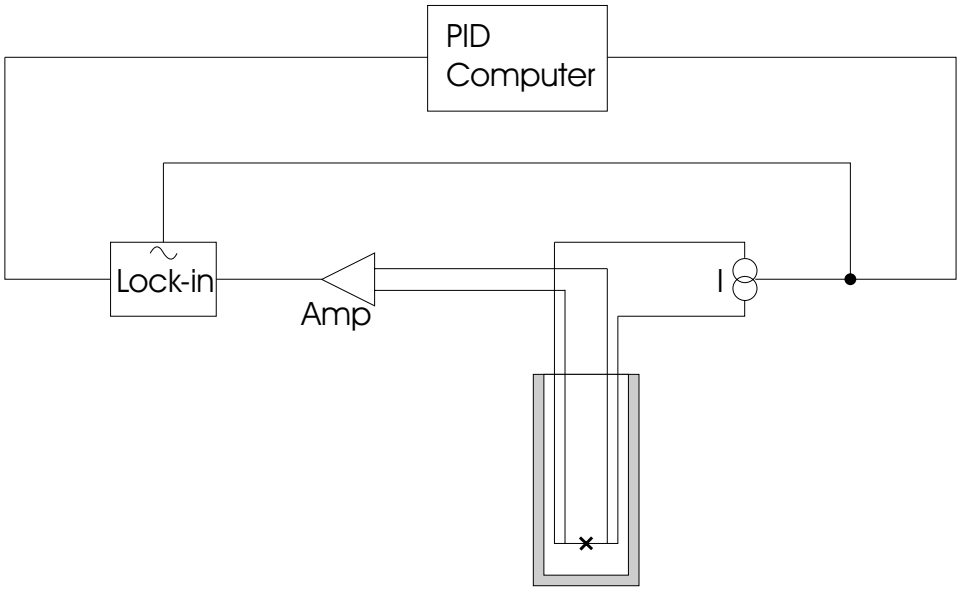

Figure 4.2: A schematic of the electronics used to measure the junction critical current. A lock-in amplifier is used to measure the slope of the IV curve and a computer controlled PID maintains the *dc* current bias.

Chapter 5

Junction Transport Measurements

The critical current has been measured as a function of temperature and applied magnetic field for grain boundary Josephson junctions of two different cuprate materials with several different dopants. The results of these measurements are outlined in this Chapter and compared to the predictions of the simple model outlined in Chapter 3.

5.1 $YBa_2Cu_3O_{7-\delta}$

The characteristics of a grain boundary Josephson junction are determined by the relative angle between the grains and the faceting caused by competing growth islands. At small orientation angles between the grains, the facets in the boundary have a lesser effect on the diffraction pattern by producing an inhomogeneous critical current density across the junction. This is caused by the anisotropy of the d-wave order parameter and disorder effects at the grain boundary both of which will depend on the facet angle. The sign change, intrinsic to the d-wave order parameter, will only affect facets with a large angle with respect to the substrate grain boundary. The diffraction patterns of low angle junctions will show deviations from the expected Fraunhofer pattern in the form of increased structure in the diffraction peaks at non-zero fields. The overall shape of the diffraction pattern, however, is maintained with the largest critical current occurring at zero applied magnetic field. Figure 5.1 shows two diffraction patterns of YBCO junctions on a 24° symmetric bicrystal. Both

the a) 15 micron and the b) 20 micron junctions have a large peak at zero field that is twice the width of the other peaks. The largest critical current occurs at zero applied magnetic field and the overall critical current decreases with increasing field. The deviations from the Fraunhofer pattern are consistent with large inhomogeneities in the critical current density with few or no sign changes. These diffraction patterns were measured at 87K to eliminate asymmetries due to self field effects. At this temperature the critical current is sufficiently reduced to put the junction in the short-junction limit.

For large angle grain boundaries the sign change of the d-wave order parameter is the dominant effect determining the junction characteristics. Adjacent facets with critical currents of different sign cancel each other, significantly reducing the magnitude of the junction critical current. The diffraction patterns are highly structured with the largest critical currents occurring at non-zero magnetic fields. Figure 5.2 shows diffraction patterns for 15 micron a) and 20 micron b) YBCO junctions with 45° asymmetric junction geometry. The largest critical currents occur at applied field currents of ± 65 mA in a) and ± 19 mA in b).

The onset of a complex order parameter is predicted to significantly increase the asymmetry of the diffraction pattern of a 45° asymmetric grain boundary junction as outlined in chapter 3. Figure 5.2 b) shows no significant change in asymmetry between a diffraction pattern taken at 15.4K and one taken at 1.5K. This is the temperature range over which a transition is expected from quasiparticle tunneling data. The minor asymmetries in the patterns are unchanged with temperature indicating they originate from a systematic error in the measurement such as stray field or trapped flux away from the junction. The structure of these diffraction patterns are consistent with a faceted grain boundary junction with pure d-wave pairing symmetry.

Figure 5.2 a) has a significant asymmetry near zero field that increases as the sample is cooled from 22K to 4.2K. This asymmetry is characterized by a local minimum in the diffraction pattern that moves to higher magnetic field values at lower temperature. An asymmetry characterized by features shifting with temperature is consistent with the onset of a complex order parameter as determined by the simulations. To determine the origin

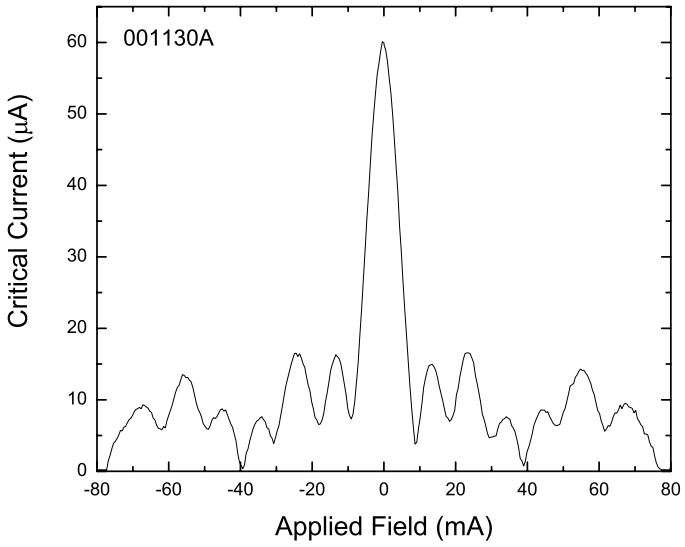

a)

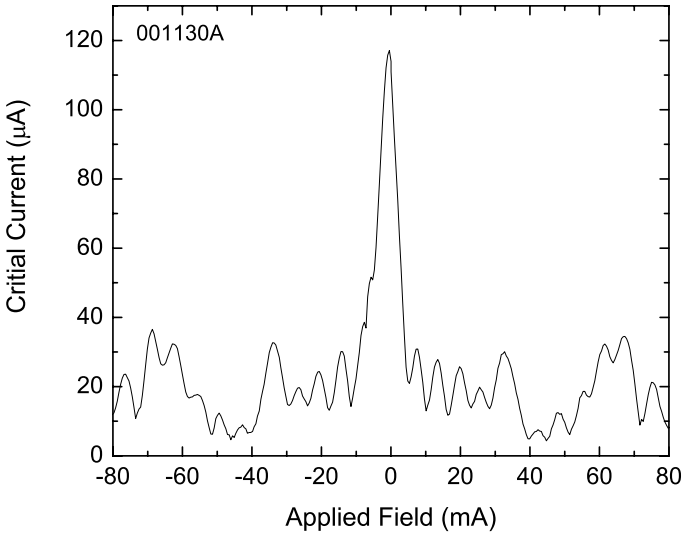

b)

Figure 5.1: Diffraction patterns for a a) 15 micron and b) 20 micron YBCO junctions on a 24° symmetric STO substrate.

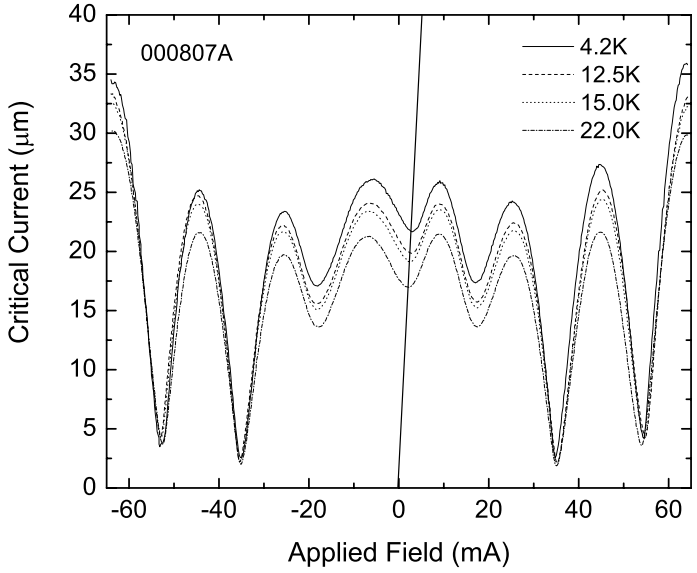

a)

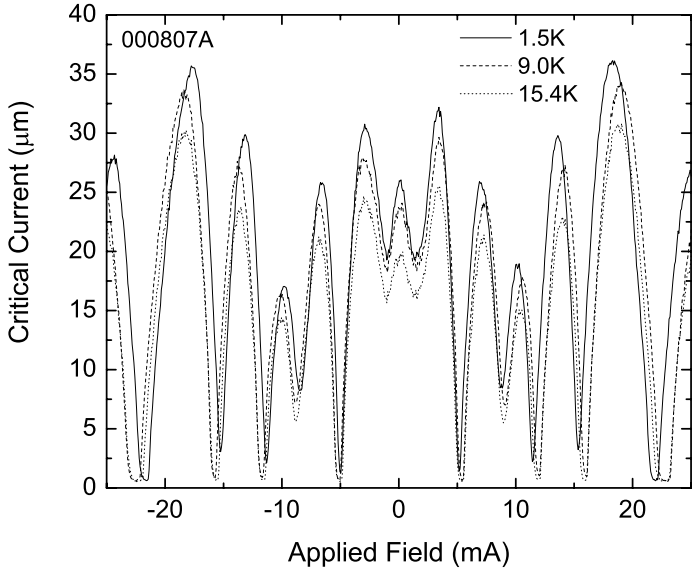

b)

Figure 5.2: Diffraction patterns for a a) 15 micron and b) 20 micron YBCO junctions on a 45° asymmetric STO substrate. A line is drawn through the first minima in a) showing that the asymmetry extrapolates through zero consistent with self-field effects .

of the asymmetry, a straight line has been added to the figure that passes through the first minimum of the diffraction patterns. This line runs through the origin indicating that the asymmetry is proportional to the critical current and is likely due to self-field effects in the junction, not a broken TRS state.

Measurement of the negative critical current diffraction pattern can test for broken TRS in these systems. Reversing the currents in the system (including those in the Helmholtz coil) is equivalent to reversing time. Asymmetries due to self field effects do not break TRS and would therefore be symmetric through the origin. An asymmetry arising from a complex order parameter and a true broken TRS state would be possess reflection symmetry through the x-axis. The negative diffraction patterns were not measured for the junctions in Fig. 5.2 but the extrapolation of a particular feature through the origin is sufficient to indicate the presence of self-field effects. In addition, the onset of asymmetry in the 15 micron junction is not reproduced in the 20 micron junction indicating a source characteristic of only the smaller junction.

The fact that the 15 micron junction shows self-field effects while the larger 20 micron junction does not is an example of the difficulty with the definition of the Josephson penetration depth in the presence of non-uniform current densities. The two junctions with identical film properties are governed by the details of the barrier. A section of the junction with large critical current density will introduce magnetic fields into neighboring regions of the junction causing asymmetries in the diffraction pattern. If the details of the barrier are unknown the junction must be measured to determine if self-fields will be a problem.

The simulations of the grain boundary Josephson junctions indicate that the onset of a complex order parameter will also cause a large jump in the critical current at zero field. It is clear from the diffraction patterns in Fig. 5.2 that there is no large increase in the critical current as the temperature is lowered. Figure 5.3 shows the critical current for a 10 micron YBCO junction on a 45° asymmetric STO substrate plotted as a function of temperature from 3K to 30K. The critical current decreases with increasing temperature in a smooth continuous fashion consistent with measurements on other grain boundary junctions.[75]

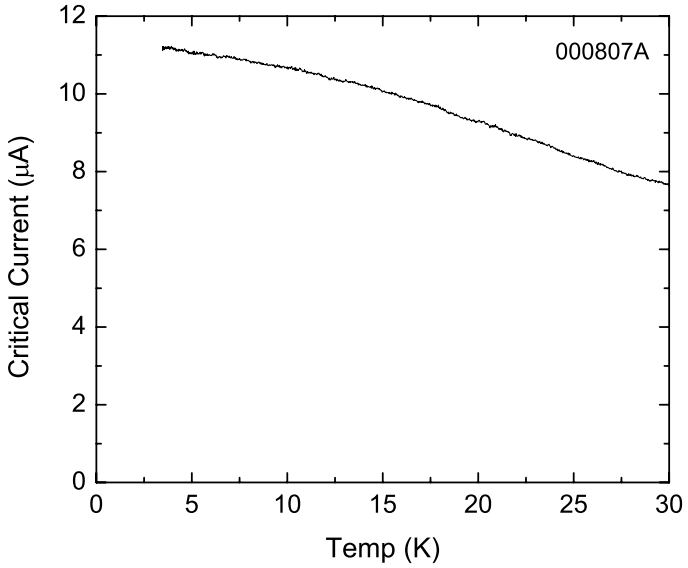

Figure 5.3: The critical current at zero applied magnetic field plotted as a function of temperature for a 10 micron YBCO junction on a 45° asymmetric STO substrate.

5.2 Ni-doped $YBa_2Cu_3O_{7-\delta}$

To test for the onset of a complex order parameter due to magnetic impurities Ni-doped YBCO junctions were measured. Films with 3% and 5% Ni substitution for Cu were fabricated and cooled to mK temperatures. Figure 5.4 shows the diffraction patterns for a) 5 micron, b) 10 micron, and c) 15 micron 45° asymmetric junctions from 20K to 340mK with 5% Ni doping. Both the 5 micron and the 15 micron junction show no increased asymmetry with decreasing temperature. The 10 micron junction shows an increased asymmetry near zero field with decreasing temperature. This asymmetry is again consistent with self-field effects in the junction brought on by the details of the non-uniform critical current density. Figure 5.5 shows the diffraction patterns for a 20 micron, 45° asymmetric junction from 22K to 3K with 3% Ni doping. There is no increased asymmetry with decreasing temperature.

The drop in thermal conductivity in the Ni-doped BSCCO single crystals was observed at milli-Kelvin temperatures. These Ni-doped YBCO junctions were cooled in a dilution refrigerator to reach lower temperature in search of the expected transition. Figure 5.6

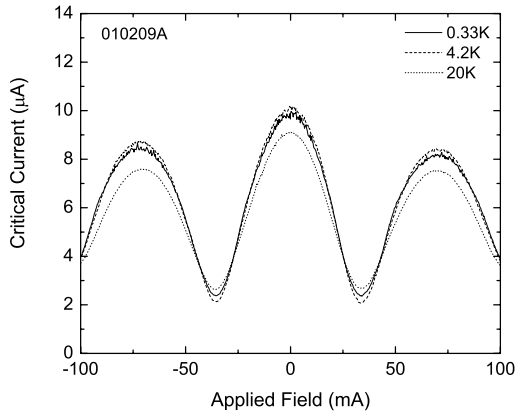

a)

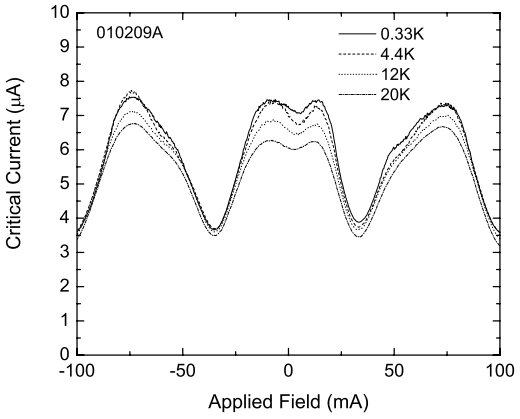

b)

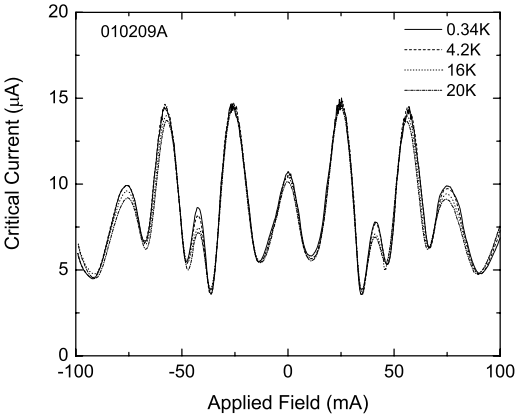

c)

Figure 5.4: Diffraction patterns for a a) 5 micron, b) 10 micron, and c) 15 micron 5% Ni-doped YBCO junctions on a 45° asymmetric STO substrate.

shows the diffraction patterns for a a) 15 micron 5% Ni-doped YBCO junction and a b) 16 micron 3% Ni-doped YBCO junction b). The 15 micron junction in Fig. 5.6 a) shows no increased asymmetry upon cooling from 4.2K down to 160mK, consistent with a pure d-wave symmetry. This 15 micron junction is the same as the junction whose higher temperature data is shown in Fig. 5.4 c). There is a clear change in the magnetic field scales between the two data sets even though the same coil was used in both measurements. This higher temperature data was taken in the ^{3}He insert where the field was suppressed by the Pb shield in close proximity to the Helmholtz coil. The suppression of the magnetic field was not discovered until the higher temperature data was compared to data taken in the dilution refrigerator, which has no Pb shield. All magnetic field scales have been left in units of milliamps because the coil calibration is not valid in all data sets.

The diffraction patterns in Fig. 5.6 b) for the 16 micron 3% Ni-doped YBCO junction show no increase in asymmetry upon cooling from 5K to 100mK. This is again consistent with a pure d-wave pairing symmetry over the entire temperature range measured. The diffraction patterns for this junction are significantly more noisy that others. This is due to a small hole or dead area in the YBCO film at the junction barrier creating a *dc*-SQUID. When measured on a smaller field scale, SQUID oscillations are observed superimposed atop the junction diffraction pattern resulting in the noise seen.

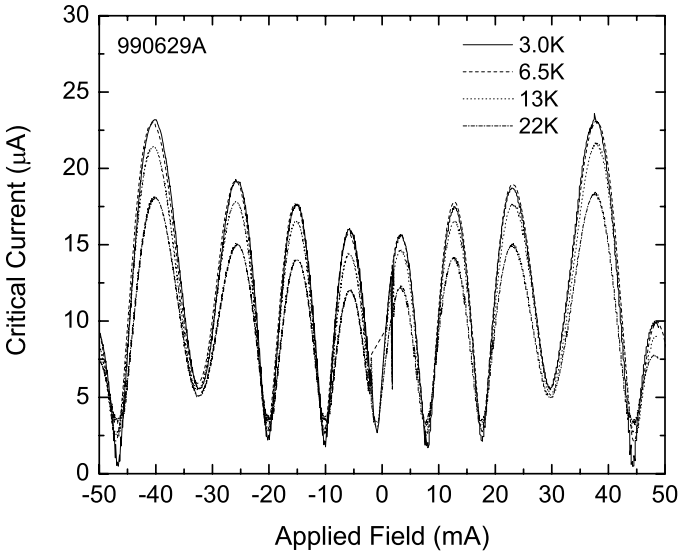

Figure 5.5: Diffraction patterns for a 20 micron 3% Ni-doped YBCO junctions on a 45° asymmetric STO substrate.

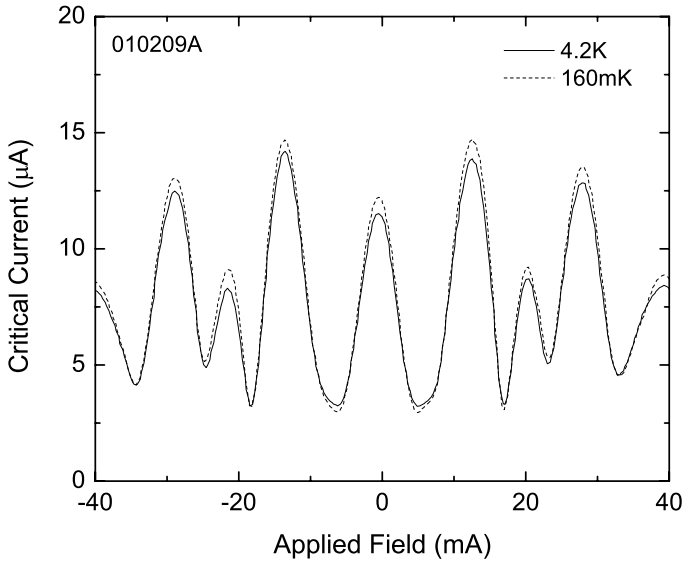

a)

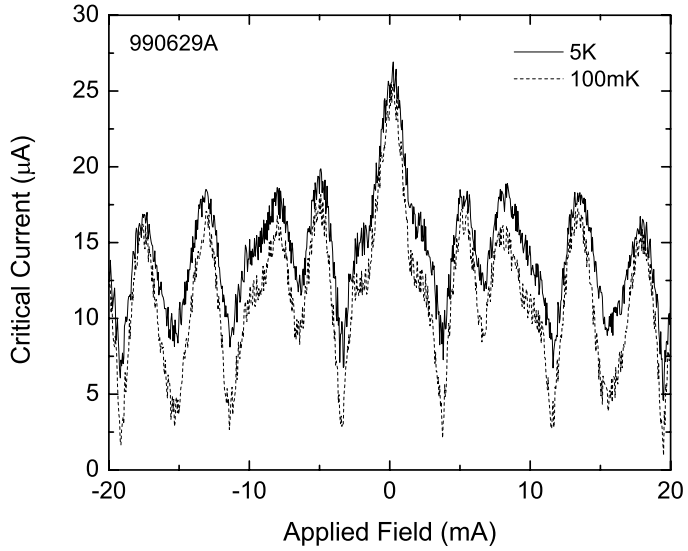

b)

Figure 5.6: Diffraction patterns for a 15 micron 5% Ni-doped YBCO junction a) and a 16 micron 3% Ni-doped YBCO junction as measured in a dilution refrigerator. There is no increased asymmetry in the diffraction patterns of the 5% and 3% doped junctions upon cooling to 160mK and 100mK respectively.

5.3 Pr-doped $YBa_2Cu_3O_{7-\delta}$

Conductance measurements on quasiparticle tunnel junctions indicate that the zero-bias conductance peak, seen in pure YBCO films, is reduced with increased Pr substitution for Y.[76] The zero-bias conductance peak disappears all together for a doping level of 50% and superconductivity is completely suppressed for doping levels around 55%. Measurement of the resistance as a function of temperature suggest that increased Pr concentration destroys the superconductivity by removing carriers consistent with underdoping with oxygen.[76] For these reasons, Pr-doped YBCO is an interesting choice to study impurity effects on the grain boundary junction properties.

Figure 5.7 a) shows diffraction patterns for a 10 micron 20% Pr-doped YBCO film on a 45° asymmetric STO substrate over a temperature range of 40K to 4.2K. There is an increase in asymmetry in the diffraction pattern with decreasing temperature. Figure 5.7 b) shows the positive and negative diffraction patterns taken at 4.2K showing that features in the patterns are symmetric through the origin. This indicates that the asymmetry is due to self-field effects. Figure 5.8 shows the positive and negative diffraction patterns for a 5 micron junction over a temperature range of 40K to 4.K. This junction also shows asymmetries in the diffraction patterns that are consistent with self-field effects. This non-Fraunhofer diffraction pattern, even with the self-field asymmetries, indicates that the 20% Pr-doped YBCO has d-wave pairing symmetry over the entire temperature range. Any change in order parameter symmetry would have a dramatic effect on the shape of the diffraction pattern. This shows that the suppression of the zero-bias conductance peak in tunnel junctions is not due to a fundamental change in the superconducting state.

Junctions of 50% Pr-doped YBCO have also been fabricated and measured. The critical currents of the grain boundary Josephson junctions were suppressed significantly rendering the feedback method of critical current measurement unusable. Conductance measurements at zero bias as a function of magnetic field have been performed. This is not a direct measurement of the critical current but scales with it in junctions with low critical currents.

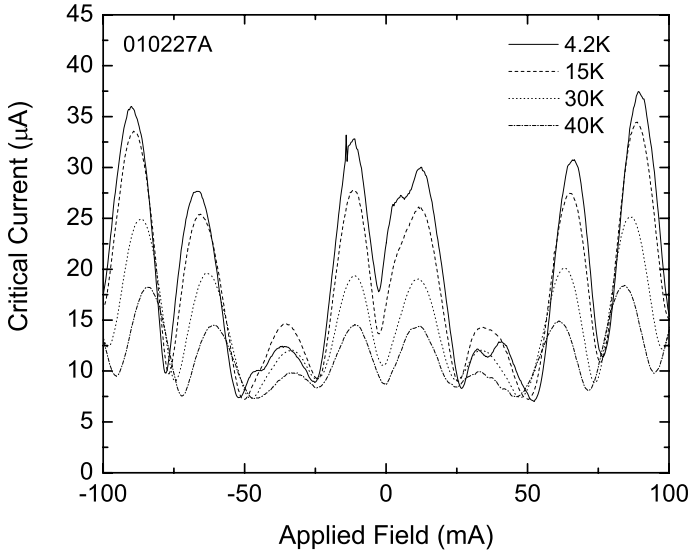

a)

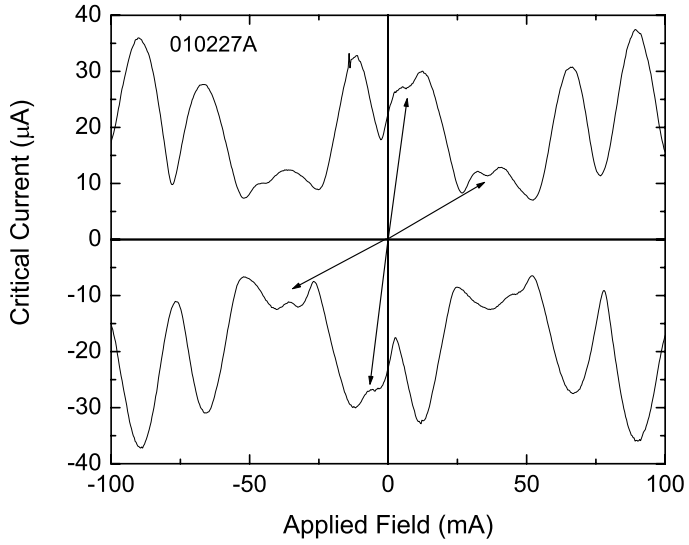

b)

Figure 5.7: a) Diffraction patterns for a 10 micron 20% Pr-doped YBCO junction on a 45° asymmetric STO substrate. b) The positive and negative diffraction patterns taken at 4.2K showing the asymmetry is symmetric through the origin.

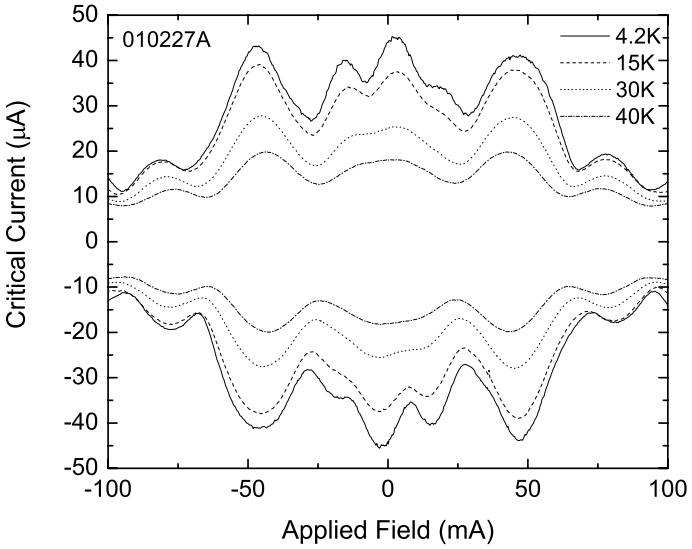

Figure 5.8: Positive and negative diffraction patterns for a 5 micron 20% Pr-doped YBCO junction on a 45° asymmetric substrate. The asymmetry that appears at lower temperature is symmetric through the origin.

These measurements are not shown here but indicate a non-Fraunhofer symmetric diffraction pattern consistent with pure d-wave pairing.

5.4 Ca and Co-doped $\mathbf{YBa_2Cu_3O_{7-\delta}}$

Quasiparticle tunneling measurements have shown that the character of the zero-bias conductance peak is dependent on the doping of the cuprate material. Krupke and Deutscher found that the zero-bias conductance peak does not split with decreasing temperature down to 4.2K for underdoped YBCO sample while optimally doped samples show a zero-field splitting below 6K. In contrast, Ca doped samples that are in the overdoped regime have no zero-bias conductance peaks at all.[47] Oxygen loss at the grain boundary resulting in an underdoped interface could suppress the onset of a complex surface symmetry. Overdoping the grains compensates for the naturally underdoped grain boundary.

The microstructure of the grain boundary reduces the doping at the interface producing space-charge layers and band bending that contribute to the reduction of the critical

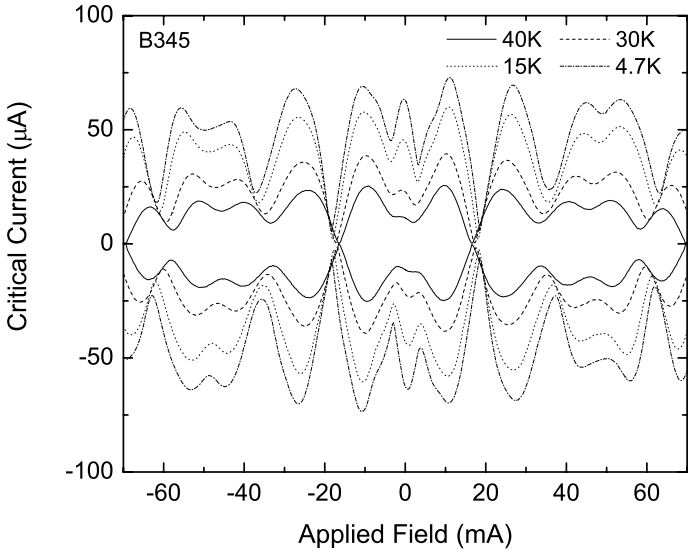

Figure 5.9: Positive and negative diffraction patterns for a 15 micron 30% Ca-doped YBCO junction on a 45° asymmetric STO substrate.

current across the boundary. These effects are present in the cuprate materials because of the decreased carrier densities resulting in longer electrostatic screening lengths similar to semiconductors. Substitution of Ca^{2+} for Y^{3+} in YBCO has been shown to increase the critical current density across 24° symmetric grain boundaries. This substitution overdopes the grains reducing the electrostatic screening length and the width of the space-charge layer. In the grain boundary the excess charge is reduced lowering the barrier potential. Substitution of Co^{3+} for in-chain Cu^{2+} has the opposite effect reducing the critical current across the grain boundary. This substitution underdopes the grains and increases the excess charge at the boundary.[18; 54; 55; 61; 77]

Figure 5.9 shows the positive and negative diffraction patterns for a 15 micron 45° asymmetric junction of 30% Ca-doped YBCO. 30% Ca doping produces the largest increase in critical current density across a 24° symmetric grain boundary.[61] The magnitude of the critical current is approximately a factor of three larger than that of the comparable pure YBCO junction shown in Fig. 5.2 a), consistent with increased critical current density seen in 24° symmetric junctions. The diffraction patterns show small asymmetries as the sample

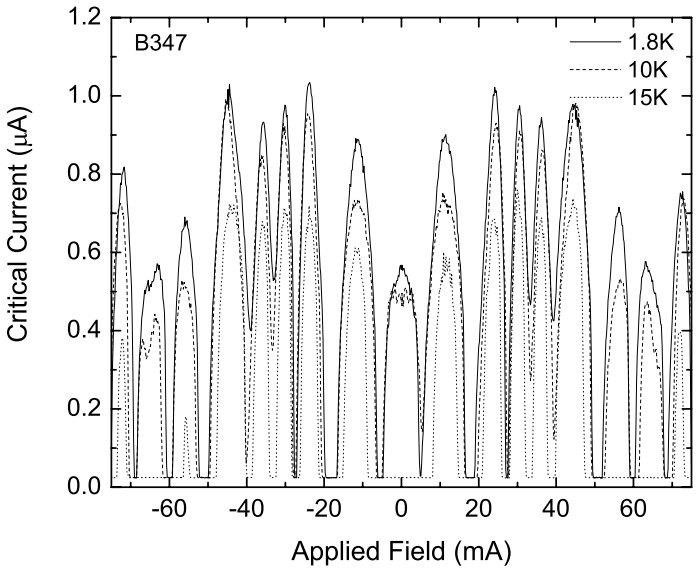

a)

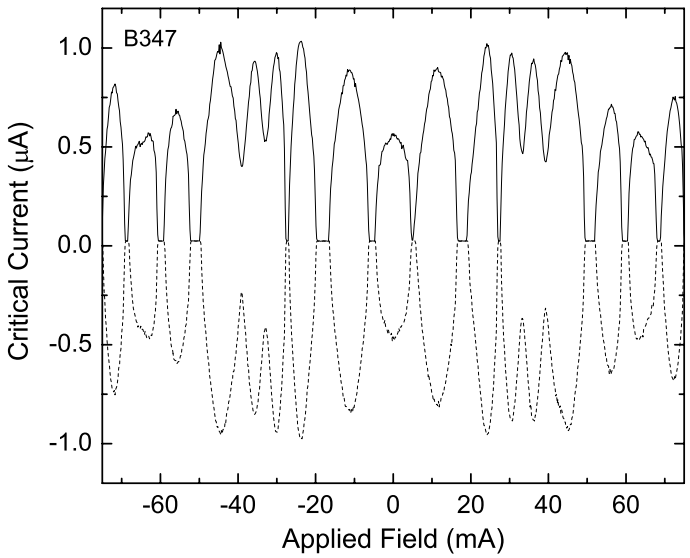

b)

Figure 5.10: a) Diffraction patterns for a 20 micron 10% Co-doped YBCO junction on a 45° asymmetric STO substrate. b) The positive and negative diffraction patterns taken at 1.8K.

is cooled from 40K down to 4.7K. All of these features are inversion symmetric, consistent with self-field effects.

Figure 5.10 a) shows the positive diffraction patterns for a 20 micron 45° asymmetric junction of 10% Co-doped YBCO. The magnitude of the critical current is reduced, consistent with the Co-doping. There are no large asymmetries in the diffraction patterns as the junction is cooled from 15K down to 1.8K. Figure 5.10 b) shows the positive and negative diffraction patterns for the same junction taken at 1.8K.

5.5 $Bi_2Sr_2CaCu_2O_8$

The character of the grain boundary in a cuprate film grown on a bicrystal is determined by the energetics of the growth process and the structure of the material. BSCCO films grown by MBE are atomically flat and produce a cleaner interface at the grain boundary. The structure is also fundamentally different from YBCO and is a good check of the results obtained for different YBCO junctions. Because of the slow growth rates in MBE, the films are thinner than those fabricated by laser ablation. The critical current densities across a grain boundary are also lower than YBCO. For these reasons it is necessary to pattern larger junctions to have a measurable critical current.

Figure 5.11 a) shows diffraction patterns for a 30 micron 45° asymmetric BSCCO junction from 20K down to 1.9K. There is no large increase in asymmetry with decreasing temperature consistent with all of the diffraction patterns measured in the YBCO system. The inset shows the central portion of the diffraction patterns showing the central peak and the first two major side peaks. Arrows above the peaks indicate the width of the central peak is significantly smaller than those of the two side peaks. Fitting the central peak and a side peaks of comparable height to a Gaussian yields widths $2\sigma = 0.7$mA and $2\sigma = 1.6$mA respectively. The central peak has a modulation length in magnetic field approximately half than of the other peaks in the pattern. There are other smaller peaks near zero field that also appear to have half modulation lengths. The central peak also has a different temperature dependence from the other peaks in the diffraction pattern. Figure 5.11 b) shows the

peak heights for several peaks in the pattern including the central peak all normalized to their value at 1.9K. All of the side peaks show the same temperature dependence regardless of peak height. The maximum critical current of the central peak decreases more rapidly with increasing temperature. Half width peaks at zero field with similar temperature behavior have also been observed in Pb-In/Ag/YBCO ramp edge Josephson junctions oriented within 15° of the $(\overline{1}\,\overline{1}\,0)$ direction. Diffraction patterns with a small or no central peak show a dramatic rise in critical current at zero applied magnetic field when the junction is cooled below 4.5K.[78]

Measuring the asymmetry in the diffraction patterns of a real grain boundary junction is complicated by several factors. A diffraction pattern can be shifted due to stray magnetic fields in the dewar resulting in an increase in measured asymmetry even for symmetric patterns. Many of the measured diffraction patterns show slight asymmetries in peak height, location, and width. Correcting for these errors is very difficult and the resulting asymmetry measurement can depend on how the corrections are made. Lastly, a measured diffraction pattern covers finite field values and usually contains a relatively small number of peaks. It is difficult to determine if the pattern covers the entire region over which the pattern is asymmetric. For these reasons it is difficult to quantify the asymmetry to place an upper limit on the strength of any subdominant component, ϵ.

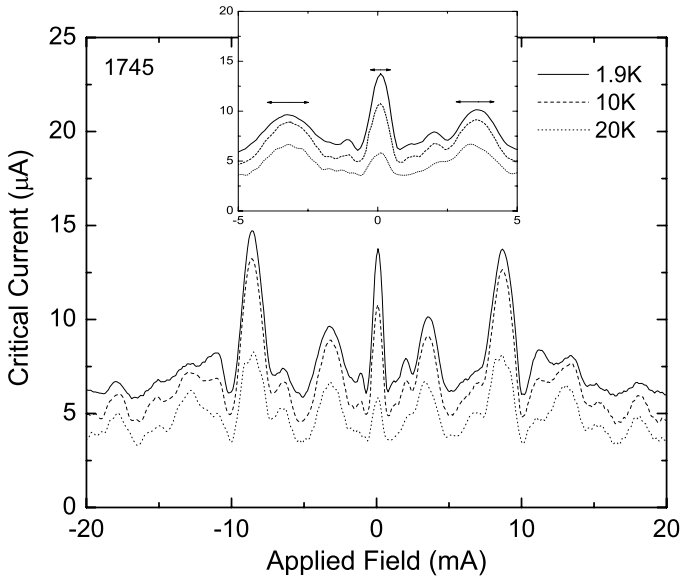

a)

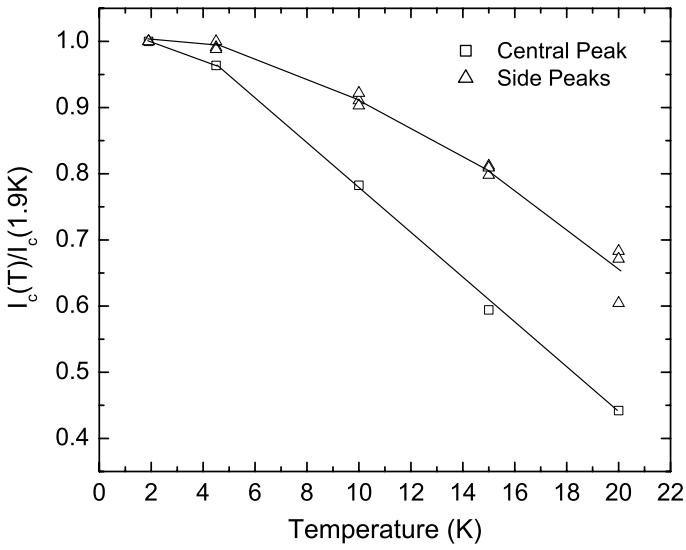

b)

Figure 5.11: a) Diffraction patterns of 30 micron MBE-grown BSCCO junction on a 45° asymmetric STO substrate. b) The central peak is half the width of the other peaks and has a different temperature dependence.

Chapter 6

Discussion

6.1 Absence of a Surface Complex Order Parameter

The simple model laid out in Chapter 3 for a faceted grain boundary Josephson junction indicates that the junction properties should be sensitive to transitions to a complex order parameter. Specifically, a complex order parameter will induce asymmetries with respect to magnetic field in the junction diffraction patterns that are not symmetric under time reversal. Such asymmetries will not be inversion symmetric when the positive and negative diffraction patterns are compared. The fully gapped complex order parameter will also cause a dramatic rise in critical current near zero applied field. This transition is expected to occur as the junction is cooled below some secondary transition temperature, consistent with quasiparticle tunneling measurements showing a splitting of the zero-bias conductance peak with cooling. Some of the junction diffraction patterns measured here show a large increase in asymmetry consistent with a complex transition but in all cased the features prove to possess TRS, consistent with self-field effects.

This null result could be due to barrier properties intrinsic to the grain boundary. Quasiparticle tunneling measurements are very sensitive to the surface quality and the doping of the cuprate material. Secondly, the formation of complex domains at the surface could wash out the order parameter's effect on the diffraction patterns. These two possibilities are discussed below.

6.1.1 Complex Domains

It is plausible that the formation of complex domains of opposite chirality (ie. $d + id$ and $d - id$) could reduce the effects of the complex transition on the junction characteristics. Spatially separate domains of opposite chirality could form simultaneously as the junction cools below the complex transition temperature. These surface domains would be strongly coupled with a large domain wall energy, of order of the Josephson energy, but this does not preclude their existence. It is useful to calculate the grain boundary characteristics incorporating domains into the model. Figure 6.1 shows several calculated diffraction patterns for a randomly generated set of 30 facets with pure d-wave, $d+id$, and $d+id$ with domains. The bottom diffraction pattern with pure d-wave pairing is symmetric while the diffraction pattern for $d + id$ pairing shows large asymmetry with an increase in the zero field critical current. Domains are randomly added to both sides of the junction independent of the faceting and diffraction patterns are calculated for 2 to 1000 domains. Since the junction contains 30 facets, this range of domain number examines the case of both large and small domains relative to the size of the facets. With 2 domains the diffraction pattern changes but the asymmetry and increased zero-field critical current (compared to the pure d-wave) are still present. As the domain size approaches the facet size the zero field critical current is reduce. However, the asymmetry is still present and exists over a larger field range with decreasing facet size. In effect, small domains increase the number of facets in the junction creating better current cancellation at zero field. The large critical current increase at zero field is reduced by the domains but the diffraction pattern asymmetry will still be sensitive to a complex transition.

6.1.2 Barrier Transmission and Broken TRS

For a complex order parameter TRS is broken by an induced subdominant pairing out of phase with the dominant d-wave symmetry. This is expected to occur for interfaces with zero or low transmission such as tunnel junction and free surfaces. At these low transmission interfaces, specular reflection produces quasiparticle paths along which the

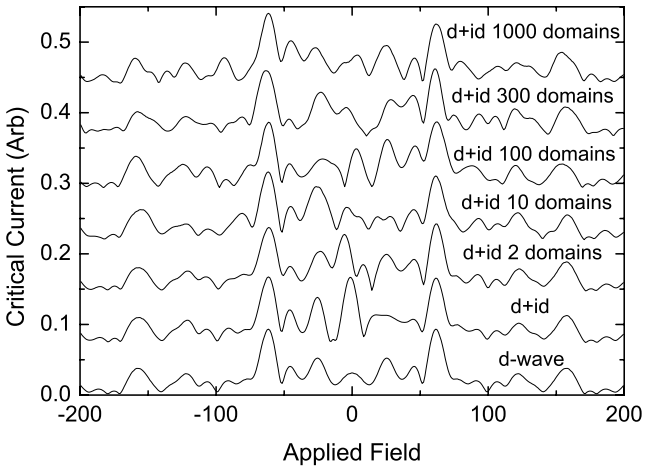

Figure 6.1: Simulated diffraction patterns for different order symmetries including pure d-wave, $d + id$, and $d + id$ with 2 to 1000 domains of opposite chirality. The domains were added independent of the facets on both sides of the barrier. Increasing the number of domains removes the large increase in critical current at zero applied magnetic field seen in the $d + id$ case with no domains. However, the asymmetry is still present.

sign of the order parameter changes. This leads to the ZEBS at the surface that are observed as the zero-bias conductance peak. These conductance peaks have been observed in grain boundary Josephson junctions as well.[79; 80] Figure 6.2 plots the conductance as a function of voltage for a 36.8° symmetric grain boundary junction from 12K to 2.5K. The zero-bias peak is clearly seen at all temperature. The dip in the peak near zero-bias is due to the critical current which was not completely suppressed, not a splitting of the peak. The observation of the zero-bias conductance peaks in the grain boundary junctions does not prove they are low transmission. The transmission coefficient for grain boundary junctions has been estimated by Fogelström et al. from measurements of the Josephson penetration depth. They calculate a transmission coefficient $|\tilde{T}|^2 \approx 10^{-4}$ for grain boundaries with misorientation angle 30°.[81] This is an averaged coefficient and may arise from a boundary with regions of high and low transmission. For the case of large angle grain boundaries with high transmission coefficients, there exist quasiparticle paths

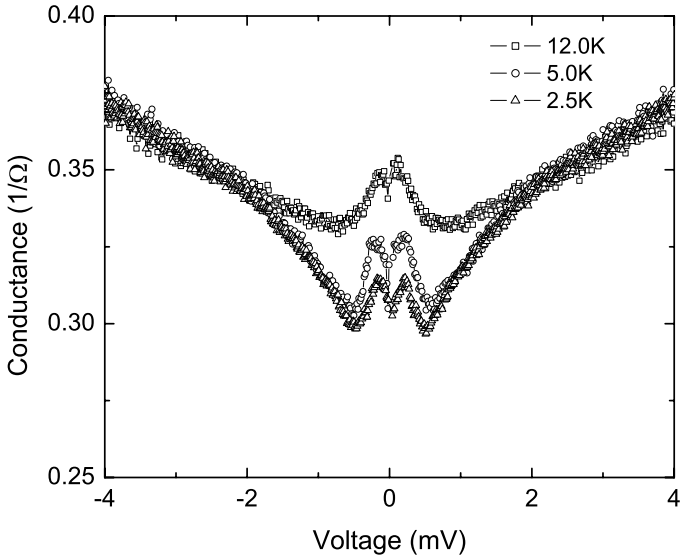

Figure 6.2: The conductance plotted as a function of voltage for a 16 micron 36.8° symmetric grain boundary Josephson junction. The zero-bias peak is clearly shown. This dip at zero voltage is due to the critical current and does not indicate a splitting of the peak.

across the junction along which the sign of the order parameter changes. Thus Andreev bound states can exist at the Fermi energy that span the barrier rather than existing at superconductor surface. It is unclear whether the barrier bound states would drive the transition to a complex surface symmetry.

Other states of broken TRS have been predicted to occur for Josephson junctions comprising two d-wave superconductors. These predictions are based on quasiclassical models that take into account surface bound state contributions to the tunneling current. The bound state currents shift the phase across the junction away from 0 to reduce the energy of the system. TRS is broken when the system chooses the phase drop $\pm\delta$. It is the junction that breaks TRS, similar to the corner SQUID and tri-crystal ring systems, in contrast to a complex order parameter where the symmetry is intrinsically broken by the surface superconducting state. Associated with this broken TRS are surface currents running along the junction whose polarity is determined by the phase across the junction.[82–84] These surface currents should also produce asymmetries in the junction diffraction patterns of

grain boundary junctions that would be indistinguishable from a complex order parameter.

6.1.3 Conclusion

The bulk d-wave order parameter that exists in the high-temperature cuprate superconductors has been predicted to break TRS at surfaces, interfaces and other scattering sites due to the intrinsic π phase shift between orthogonal k-space directions. The transport properties of 45° asymmetric grain boundary Josephson junctions are altered by broken TRS in a distinct manner regardless of the origin of the broken symmetry. This particular junction geometry creates, *in-situ*, an interface free of damage from device fabrication that is perpendicular to the (110) direction, predicted to induce broken symmetry. The transport properties of several doped and undoped YBCO junctions and an undoped BSCCO junction have been measured to test boundaries of different character. None of the measurements show conclusive evidence of a broken TRS state.

6.2 Second-Order Josephson Coupling

The subject of Josephson tunneling into superconductors with d-wave symmetry has been examined by Yip and others.[85–87]. Yip shows that the sign change in the d-wave order parameter cancels the first-order Josephson tunneling in junctions along the (110) crystal direction. The amount of cancellation may be dependent on junction barrier quality so the critical current through the junction will have the general form

$$I = I_{c_1}\sin(\phi) + I_{c_2}\sin(2\phi) + \ldots \tag{6.1}$$

where $f(n\phi) = \sin(n\phi)$ for $n = 1, 2, 3\ldots$ Each term represents tunneling processes involving n electron pairs whose tunneling probability decreases with increasing n. Cancellation of the first-order term means second-order tunneling processes, that are unaffected by the d-wave sign change, are dominant. It is important to note that the cancellation of the first-order tunneling occurs locally on flat (110) surfaces. This is not the same as the cancellation of the critical current in the corner junction experiment or in the faceted grain boundary

junctions even though they are both caused by the d-wave sign change. For this reason, the suppression of first-order tunneling will depend on the interface roughness.

It has been shown here that the transport properties of large-angle grain boundary Josephson junctions are dominated by a faceted interface caused by competing growth islands. However, it is plausible that a grain boundary grown on a bi-crystal substrate by MBE will have smaller scale deviations from the substrate boundary due to the nature of the growth process. Such a boundary would decrease first-order tunneling effects allowing higher order terms to dominate. The diffraction patterns in Fig. 5.11 a) for the 45° asymmetric BSCCO junction indicate a large peak at zero applied magnetic field with approximately half the width of the other peaks. Both the peak width and location are consistent with the second-order tunneling term in (6.1) with a modulation length π. Because the second-order tunneling is unaffected by the d-wave sign change, it contributes a Fraunhofer-like critical current component that is added to the largely non-Fraunhofer first-order component to produce the junction diffraction pattern. Second-order tunneling effects therefore appear strongest at zero field. The normalized critical current peak heights plotted in Fig. 5.11 b) indicate the central peak decreases more rapidly with increasing temperature than the other peaks in the diffraction pattern. The single pair tunneling involves terms in the tunneling Hamiltonian M^2 where M is the tunneling matrix element. From Ginzburg-Landau theory, near T_c these tunneling processes depends linearly on temperature, $(T - T_c)$. Second-order tunneling terms M^4 and depend quadratically on temperature, $(T - T_c)^2$. While these results are only valid near T_c they indicate the second-order tunneling should drop more rapidly with increasing temperature than first-order.

Second-order tunneling is not the only source of a possible $\sin(2\phi)$ component to the current-phase relationship, $f(\phi)$. This function is only constrained to be 2π periodic. It was mentioned in Section 1.3 that $f(\phi) = \sin(\phi)$ only for ideal barriers with a low transmission coefficient. Calculations of $f(\phi)$ for superconducting bridge weak links show significant deviations from the ideal barrier case.[88–90] However, these non-sinusoidal components are first-order and would not change in relative strength with changing temperature.

6.2.1 Current-Phase Measurements

The form of the current-phase relationship for grain boundary Josephson junctions in cuprate materials has been extensively studies by Il'ichev et al.[91–93] They find significant departure from the sinusoidal form for symmetric and asymmetric 45° grain boundary junctions. The measurements were made using a well characterized tank circuit with an *rf* drive-current inductively coupled to a superconducting loop containing the junction (an *rf*-SQUID). Figure 6.3 a) shows a schematic of the measurement circuit with the junction being measured is labelled JJ. Information about the current in the loop is obtained by careful measurement of the phase angle, α, between the drive current I_{rf} and the voltage across the tank circuit as a function of dc flux in the superconducting loop. The phase angle is related to the flux by

$$\alpha(\Phi_{dc}) = \frac{k^2 Q \beta_L \dot{f}(\Phi_{rf} + \Phi_{dc})}{1 + \beta_L \dot{f}(\Phi_{rf} + \Phi dc)} \tag{6.2}$$

where k is the coupling factor describing the mutual inductance between the tank circuit and the SQUID loop, Q is the quality factor of the tank circuit, $\dot{f}(\Phi) = df(\Phi)/d\Phi$ is the derivative of the current phase relationship. Figure 6.3 b) shows the current-phase relationship for two different 45° symmetric junctions for different temperature using this method. Each junction shows a distinct departure from sinusoidal at the lower temperatures. The authors ascribe the discrepancies between the two measurements to different junction characteristics such as grain boundary quality and cross sectional area.

The *rf* technique for measuring the current-phase relationship requires minimal sample fabrication. The junction being measured is incorporated into a superconducting loop with $\beta_L < 1$ and inductively coupled to the tank circuit. However, there is some danger in performing these measurements on bi-crystal grain boundary junctions which necessarily must have two junctions in the superconducting loop. This problem can be overcome by engineering the second junction such that $I_{c_1} \ll I_{c_2}$ so that any phase drop happens across the junction of interest. This is typically done by increasing the junction area(or length). But this does not work for the special case of 45° asymmetric grain boundary

a)

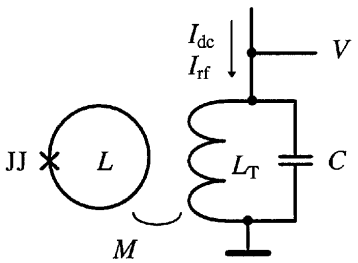

b)

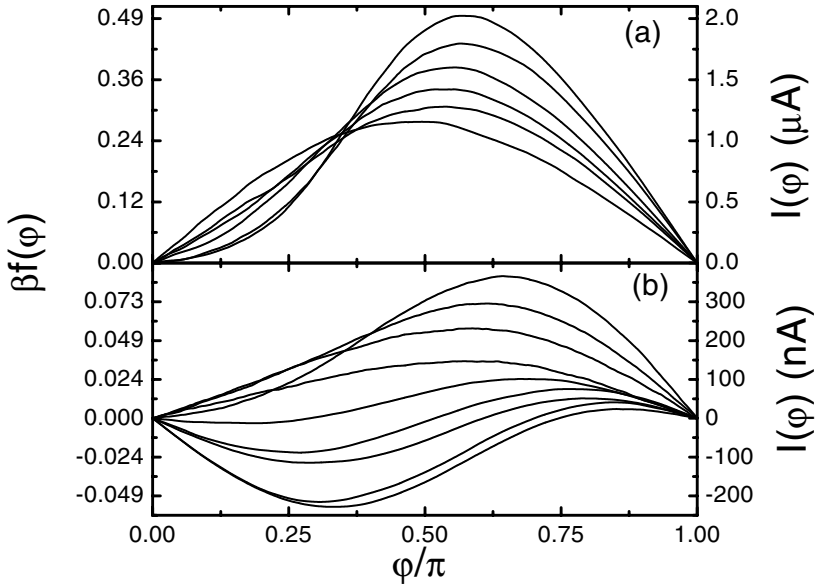

Figure 6.3: a) A circuit diagram of the Josephson junction loop and the tank circuit used in the *rf* measurement of the current-phase relationship. b) The critical current plotted as a function of phase for two different 45° asymmetric YBCO grain boundary junctions.

a)

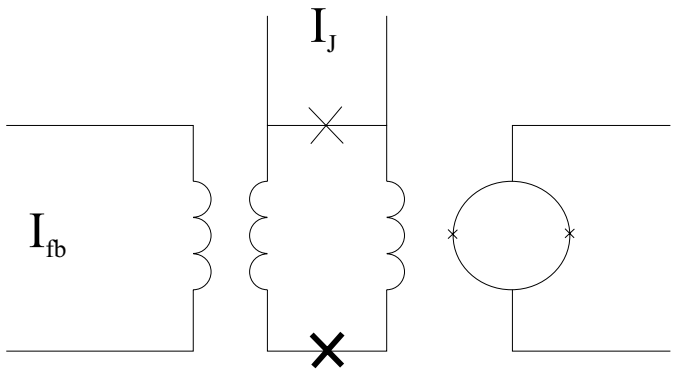

b)

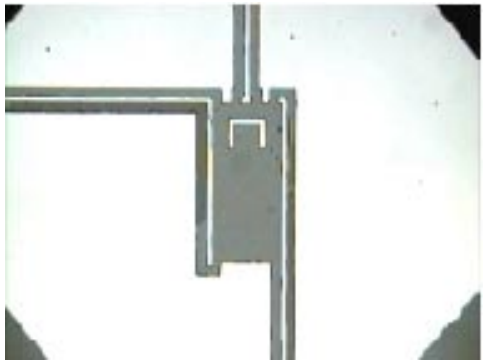

Figure 6.4: a) A diagram of the *dc* current-phase measurement circuit. b) A picture of a realization of the circuit shown in a) with YBCO bi-crystal grain boundary junctions. The grain boundary junction runs vertically through the central loop between the current leads. The small size scale is necessary to keep the loop inductance low but makes the magnetic de-coupling of the different parts of the circuit difficult.

junctions where the cancellation due to faceting produces a zero field critical current that is independent of the junction area. In this case a *dc* measurement of the critical current is required. The *dc* measurement method is outlined by Waldram and Lumley[94] who used the technique on SNS junctions of Pb and Cu. In this configuration, the junction is built into the measurement circuit and a *dc* SQUID is used to detect current circulating in the junction loop. Figure 6.4 a) shows a diagram of the circuit with the SQUID detector and a flux feedback coil. The secondary junction that is not being tested is shown as a thick cross at the bottom of the loop. Current I sent into the loop will split between the loop, I_L, and the junction, I_J. Flux is fed back into the junction loop to null out I_L. Then the feedback current is proportional to the phase across the junction, ϕ, and $I_J = I$. While the *dc* technique is more straightforward, it is more difficult because there are several sources

of flux in the system. It is important that the feedback flux couple only to the junction loop and not to the junction directly or to the SQUID. To gain access to the current-phase relationship over the full phase range 0 to π requires $\beta_L < 1$. These requirements are difficult to fulfill with cuprate grain boundary Josephson junctions due to the planar geometry of the samples. Figure 6.4 b) shows a picture of a *dc* current-phase measurement circuit fabricated out of YBCO on a bi-crystal substrate. The feedback and SQUID detector are incorporated directly into the junction loop for simplicity.

6.3 Future Work

There is an ongoing effort in our lab to measure the current-phase of a 45° asymmetric cuprate grain boundary junction using the *dc* technique. I hope to perform this measurement on MBE grown BSCCO films shortly. There are still several signal strength and de-coupling problems to overcome that arise from the planar nature of the grain boudary circuits. Shapiro step measurements are also planned to look for evidence of second-order tunneling. If successful, these measurements could provide definitive evidence of the second-order Josephson tunneling indicated in the BSCCO diffraction pattern measurements.

After my thesis exam I plan to stay in Urbana for a few months as a post-doctoral researcher to complete these measurements.

Appendix A

Film Characteristics

Table A.1 contains the information on the superconducting transition for each sample used in this study including the transition temperature, transition width, and the method of measurement. Also listed are the sample stoichiometries and the grain boundary orientations.

Table A.1: Data on the film properties prior to device fabrication. T_c gives the transition temperature and ΔT indicated the width of the superconducting transition. Also indicated is the measurement method. n/a indicates that data is not available.

Sample ID	Material	Substrate	T_c (K)	ΔT (K)	Method	Notes
001130A	$YBa_2Cu_3O_{7-\delta}$	$24°Sym.SrTiO_3$	90.5	3	ac inductance	
000807A	$YBa_2Cu_3O_{7-\delta}$	$45°Asym.SrTiO_3$	90.5	2	ac inductance	
980723B	$YBa_2Cu_3O_{7-\delta}$	$45°Sym.SrTiO_3$	90	5	ac inductance	
990401A	$YBa_2Cu_{2.91}Ni_{0.09}O_{7-\delta}$	$45°Asym.SrTiO_3$	69.5	3	ac inductance	
990625A	$YBa_2Cu_{2.91}Ni_{0.09}O_{7-\delta}$	$45°Sym.SrTiO_3$	n/a	n/a	inductive	data file lost
990629A	$YBa_2Cu_{2.91}Ni_{0.09}O_{7-\delta}$	$45°Asym.SrTiO_3$	72.5	3	ac inductance	
010209A	$YBa_2Cu_{2.85}Ni_{0.15}O_{7-\delta}$	$45°Asym.SrTiO_3$	80	8	ac inductance	
001103A	$Y_{0.5}Pr_{0.5}Ba_2Cu_3O_{7-\delta}$	$45°Asym.SrTiO_3$	n/a	n/a	inductive	
010131A	$Y_{0.5}Pr_{0.5}Ba_2Cu_3O_{7-\delta}$	$45°Asym.SrTiO_3$	20	4	resistive	
010227A	$Y_{0.8}Pr_{0.2}Ba_2Cu_3O_{7-\delta}$	$45°Asym.SrTiO_3$	n/a	n/a	n/a	
B345	$Y_{0.7}Ca_{0.3}Ba_2Cu_3O_{7-\delta}$	$45°Asym.SrTiO_3$	71	3	resistive	
B347	$YBa_2Cu_{2.9}Co_{0.1}O_{7-\delta}$	$45°Asym.SrTiO_3$	79.5	2	resistive	
1706	$Bi_2Sr_2CaCu_2O_8$	$45°Asym.SrTiO_3$	84	8	resistive	
1745	$Bi_2Sr_2CaCu_2O_8$	$45°Asym.SrTiO_3$	78	15	resistive	
1795	$Bi_2Sr_2CaCu_2O_8$	$45°Asym.SrTiO_3$	59	8	resistive	

References

[1] R. P. Feynman, R. B. Leighton, and M. Sands. *The Feynman Lectures on Physics Volume III* (Addison-Wesley Publishing Co., 1989).

[2] J. S. Townsend. *A Modern Approach to Quantum Mechanics* (McGraw-Hill Inc., New York, 1992).

[3] J. R. Waldram. *Superconductivity of Metals and Cuprates* (Institute of Physics Publishing, Bristol, England, 1996).

[4] C. P. Poole Jr., H. A. Farach, and R. J. Creswick. *Superconductivity* (Academic Press, New York, 1995).

[5] J. Bardeen, L. N. Cooper, and J. R. Schrieffer. "Theory of superconductivity." *Phys. Rev.* **108** 1175–1204 (1957).

[6] L. P. Goŕkov. "Microscopic derivation of the Ginzburg-Landau equations in the theory of superconductivity." *Sov. Phys. JETP* **36** 1364–1367 (1959).

[7] D. J. Van Harlingen. "Phase-sensitive test of the symmetry of the pairing state in the high-temperature superconductor–evidence for $d_{x^2-y^2}$ symmetry." *Rev. Mod. Phys.* **67** 515–535 (1995).

[8] J. Annett, N. Goldenfeld, and S. R. Renn. "Interpretation of the temperature dependence of the electromagnetic penetration depth in $YBa_2Cu_3O_{7-\delta}$." *Phys. Rev. B* **43** 2778–2782 (1991).

[9] D. J. Scalapino. "The case for $d_{x^2-y^2}$ pairing in the cuprate superconductors." *Physics Reports* **250** 329–365 (1995).

[10] B. D. Josephson. "Possible new effects in superconductive tuneling." *Phys. Lett.* **1** 251–253 (1962).

[11] B. D. Josephson. "Supercurrents through barriers." *Advances in Physics* **14** 419–451 (1965).

[12] A. J. Leggett. Private communication.

[13] Y. Ohashi. "Unusual proximity effect of d-wave superconductors." *J. Phys. Soc. Jpn.* **65** 823–839 (1995).

[14] M. Tinkam. *Introduction to Superconductivity* (McGraw-Hill, Inc., New York, 1996).

[15] N. M. Plakida. *High-Temperature Superconductivity* (Springer-Verlag, New York, 1995).

[16] D. M. Ginsberg, editor. *Physical Properties of High Temperature Superconductors IV*, pp. 67–122 (World Scientific, Singapore, 1994).

[17] D. M. Ginsberg, editor. *Physical Properties of High Temperature Superconductors II*, pp. 123–198 (World Scientific, Singapore, 1990).

[18] G. Hammerl et al. "Doping-induced enhancement of grain boundary critical currents." *IEEE Transactions on Applied Superconductivity* **11** 2830–2837 (2001).

[19] D. M. Ginsberg, editor. *Physical Properties of High Temperature Superconductors I*, p. 7 (World Scientific, Singapore, 1989).

[20] J. G. Bednorz and K. A. Müller. "Possible high T_c superconductivity in te Ba-La-Cu-O system." *Z. Phys. B* pp. 189–193 (1986).

[21] C. C. Tsuei and J. R. Kirtley. "Pairing symmetry in cuprate superconductors." *Rev. Mod. Phys.* **72** 969–1016 (2000).

[22] D. A. Wollman. *Experimental Determination of the Symmetry of the Superconducting Pairing State in YBCO.* Ph.D. thesis, University of Illinois at Urbana-Champaign (1996).

[23] D. A. Wollman, D. J. Van Harlingen, J. Giapintzakis, and D. M. Ginsberg. "Evidend for $d_x^2 - y^2$ pairing from the magnetic field modulation of $YBa_2Cu_3O_7 - Pb$ josephson junctions." *Phys. Rev. Lett.* **74** 797–800 (1995).

[24] D. A. Wollman, D. J. Van Harlingen, W. C. Lee, D. M. Ginsberg, and A. J. Leggett. "Experimental determination of the superconducting pairing state in YBCO from the phase coherence of YBCO-Pb dc SQUIDs." *Phys. Rev. Lett.* **71** 2134–2137 (1993).

[25] M. Sigrist and T. M. Rice. "Paramagnetic effect in high T_c superconductors–A hint for d-wave superconductivity." *J.Phys. Soc. Jpn.* **61** 4283–4286 (1992).

[26] C. C. Tsuei et al. "Pairing symmetry and flux quantization in a tricrystal superconducting ring of $YBa_2Cu_3O_{7-\delta}$." *Phys. Rev. Lett.* **73** 593–596 (1994).

[27] C. C. Tsuei et al. "Pairing symmetry in single-layer tetragonal $Tl_2Ba_2CuO_{6+\delta}$ superconductors." *Science* **271** 329–332 (1996).

[28] J. R. Kirtley et al. "Half-integer flux quantum effect in tricrystal $Bi_2Sr_2CaCu_2O_{8+\delta}$." *Europhys. Lett.* **36** 707–712 (1996).

[29] C. C. Tsuei and J. R. Kirtley. "Phase-sensitive evidence for d-wave pairing symmetry in electron-doped cuprate superconductors." *Phys. Rev. Lett.* **85** 182–185 (2000).

[30] A. Mathai et al. "Experimental proof of a time-reversal-invariant order parameter with a π shift in $YBa_2Cu_3O_{7-\delta}$." *Phys. Rev. Lett.* **74** 4523–4526 (1995).

[31] C.-R. Hu. "Midgap surface states as a novel signature for $d_{x^2+y^2}$-wave superconductivity." *Phys. Rev. Lett.* **72** 1526–1529 (1994).

[32] P. F. Bagwell. "Suppression of the Josephson current through a narrow, mesoscopic, semiconductor channel by a single imputiry." *Phys. Rev. B* **46** 12573–12586 (1992).

[33] L. J. Buchholtz, M. Palumbo, D. Rainer, and J. A. Sauls. "Thermodynamics of a d-wave superconductor near a surface." *J. Low Temp. Phys.* **101** 1079–1098 (1995).

[34] M. Matsumoto and H. Shiba. "Coexistence of different symmetry order parameters near a surface in d-wave superconductors i." *J. Phys. Soc. Jpn.* **64** 3384–3396 (1995).

[35] R. Shankar. *Principles of Quantum Mechanics* (Plenum Press, New York, 1994).

[36] Š. Kos. "Physical mechanism of the surface $d \to d + is$ transition." *Europhys. Lett.* **53** 246–250 (2001).

[37] Šimon Kos. "Zero-bias states and the mechanism of the surface $d \to d + is$ transition." *Phys. Rev. B* **63** 214506–214519 (2001).

[38] Šimon Kos. *Two Applications of the Quasiclassical Method to Superfluids.* Ph.D. thesis, University of Illinois at Urbana-Champaign (2001).

[39] H. Walter et al. "Low-temperature anomaly in the penetration depth of $YBa_2Cu_3O_7$ films: Evidence for Andreev bound states at surfaces." *Phys. Rev. Lett.* **80** 3598–3601 (1998).

[40] J. Geerk and G. Linker. "Electron tunneling into thin films of $Y_1Ba_2Cu_3O_7$." *Z. Phys. B* **73** 329–336 (1988).

[41] J. Lesueur, L. H. Greene, W. L. Feldmann, and A. Inam. "Zero bias anomalies in $YBa_2Cu_3O_7$ tunnel junctions." *Physica C* **191** 325–332 (1992).

[42] M. Covington et al. "Observation of surface-induced broken time-reversal symmetry in $YBa_2Cu_3O_7$ tunnel junctions." *Phys. Rev. Lett.* **79** 277–280 (1997).

[43] L. H. Greene et al. "Tunneling into high temperature superconductors: Andreev bound states and broken time-reversal symmetry." *Solid State Communications* **107** 649–656 (1998).

[44] I. Iguchi et al. "Angle-resolved Andreev bound states in anisotropic d-wave high-T_c $YBa_2Cu_3O_{7-y}$ superconductors." *Phys. Rev. B* **62** R6131–R6134 (2000).

[45] Y. Tanaka and S. Kashiwaya. "Theory of tunneling spectroscopy of d-wave superconductivity." *Phys. Rev. Lett.* **74** 3451–3454 (1995).

[46] M. Fogelström, D. Rainer, and J. A. Sauls. "Tunneling into current-carrying surface states of high-T_c superconductors." *Phys. Rev. Lett.* **79** 281–284 (1997).

[47] R. Krupke and G. Deutscher. "Spontaneous and field enhanced sub-gaps in in-plane oriented $(100) - Y_{1-x}Ca_xBa_2Cu_3O_{7-y}/In$ tunnel junctions." *J. Low Temp. Phys.* **117** 533–537 (1999).

[48] A. V. Balatsky. "Spontaneous time reversal and parity breaking in a $d_{x^2-y^2}$-wave superconductor with magnetic impurities." *Phys. Rev. Lett.* **80** 1972–1975 (1998).

[49] R. Movshovich et al. "Low-temperature anomoly in thermal conductivity of $Bi_2Sr_2Ca(Cu_{1-x}Ni_x)_2O_8$: Second superconducting phase?" *Phys. Rev. Lett.* **80** 1968–1971 (1998).

[50] S. L. Shinde and D. A. Rudman, editors. *Interfaces in High T_c Superconducting Systems*, chapter 6, pp. 176–209 (Springer-Verlag, 1994).

[51] D. Dimos, P. Chaudhari, J. Mannhart, and F. K. LeGoues. "Orientation dependence of grain-boundary critical currents in $YBa_2Cu_3O_{7-\delta}$ bicrystals." *Phys. Rev. Lett.* **61** 219–222 (1988).

[52] D. Dimos, P. Chaudhari, and J. Mannhart. "Superconducting transport properties of grain boundaries in $YBa_2Cu_3O_7$ bicrystals." *Phys. Rev. B* **41** 4038–4049 (1990).

[53] J. Mannhart and P. Chaudhari. "High-T_c bicrystal grain boundaries." *Physics Today* **54** 48–53 (2001).

[54] H. Hilgenkamp and J. Mannhart. "Superconducting and normal-state properties of $YBa_2Cu_3O_{7-\delta}$-bicrystal grain boundary junctions in thin films." *Appl. Phys. Lett.* **73** 265–267 (1998).

[55] H. Hilgenkamp and J. Mannhart. "Implications of $d_{x^2-y^2}$ symmetry and faceting for the transport properties of grain boundaries in high-T_c superconductors." *Phys. Rev. B* **53** 14586–14593 (1996).

[56] R. Gross et al. "Thermally activated phase slippage in high-T_c grain-boundary Josephson junctions." *Phys. Rev. Lett.* **64** 228–231 (1990).

[57] V. Ambegaokar and B. I. Halperin. "Voltage due to thermal noise in the dc Josephson effect." *Phys. Rev. Lett.* **22** 1364–1366 (1969).

[58] J. Mannhart et al. "Generation of magnetic flux by single grain boundaries of $YBa_2Cu_3O_{7-x}$." *Phys. Rev. Lett.* **77** 2782–2785 (1996).

[59] C. A. Copetti et al. "Electrical properties of 45° grain boundaries of epitaxial ybacuo, dominated by crystalline microstructure and d-wave-symmetry." *Physica C* **253** 63–70 (1995).

[60] D. Dijkkamp et al. "Preparation of y-ba-cu oxide superconductor thin films using pulsed laser evaporation from high T_c bulk material." *Appl. Phys. Lett.* **51** 619–621 (1987).

[61] A. Schmehl et al. "Doping-induced enhancement of the critical currents of grain boundaries in $YBa_2Cu_3O_{7-\delta}$." *Europhys. Lett.* **47** 110–115 (1999).

[62] R. Behrisch, editor. *Sputtering by Particle Bombardment II*, pp. 1–84 (Springer-Verlag, Berlin, 1983).

[63] C. B. Eom et al. "In situ grown $YBa_2Cu_3O_{7-d}$ thin films from single-target magnetron sputtering." *Appl. Phys. Lett.* **55** 595–597 (1989).

[64] L. H. Greene et al. "Off-axis sputter deposition of $YBa_2Cu_3O_7$ thin films for microwave aplications." *Appl. Phys. Lett.* **59** 1629–1631 (1991).

[65] D. E. Pugel and L. H. Greene. "Influence of target-substrate angle on the elemental concentration of c-axis $YBa_2Cu_3O_{7-\delta}$ thin films." *Appl. Phys. Lett.* **75** 1589–1591 (1999).

[66] B. W. Wessels et al., editors. *Annual Review of Materials Science*, pp. 679–709 (Annual Reviews Inc., Palo Alto, California, 1995).

[67] J. W. Ekin et al. "High T_c superconductor/noble-metal contacts with surface resistivities in the $10^{-10}\Omega cm^2$ range." *Appl. Phys. Lett.* **52** 1819–1821 (1988).

[68] W. Eidelloth and R. L. Sandstrom. "Wet etching of gold films compatible with high T_c superconducting thin films." *Appl. Phys. Lett.* **59** 1632–1634 (1991).

[69] M. F. Yan et al. "Water interaction with the superconducting $YBa_2Cu_3O_7$ phase." *Appl. Phys. Lett.* **51** 532–534 (1987).

[70] R. L. Barns and R. A. Laudise. "Stability of superconducting $YBa_2Cu_3O_7$ in the presence of water." *Appl. Phys. Lett.* **51** 1373–1375 (1987).

[71] J. A. Bonetti and J. E. Hilliard. Private communication.

[72] Oxford Instruments Scientific Research Division. *Heliox* 2^{VL} *Operator's Handbook* (1996).

[73] Oxford Instruments Scientific Research Division. *Kelvinox 25 Dilution Refrigerator Operator's Handbook* (1994).

[74] B. D. Yanoff. *Temperature dependence of the penetration depth in the unconventional superconductor* Sr_2RuO_4. Ph.D. thesis, University of Illinois at Urbana-Champaign (2000).

[75] J. A. Luine et al. "Critical current in high T_c grain boundary junctions." *J. Appl. Phys.* **84** 3972–3979 (1998).

[76] M. W. Covington. *Growth, Transport, and Tunneling Spectroscopy of* $Y_{1-x}Pr_xBa_2Cu_3O_7$ *Thin Films as a Functino of Crystallographic Orientation*. Ph.D. thesis, University of Illinois at Urbana-Champaign (1997).

[77] G. Hammerl et al. "Enhanced supercurrent density in polycrystaline $YBa_2Cu_3O_{7-\delta}$ at 77k from calcium doping of grain boundaries." *Nature* **407** 162–164 (2000).

[78] J. E. Hilliard Jr. *Conductivity and Interferometry Experiments on YBCO/Pb Ramp-Edge Josephson Junctions*. Ph.D. thesis, University of Illinois at Urbana-Champaign (2001).

[79] L. Alff et al. "Observation of bound surface states in grain-boundary junctions of high-temperature superconductors." *Phys. Rev. B* **58** 11197–11200 (1998).

[80] L. Alff et al. "Andreev bound states in high temperature superconductors." *Eur. Phys. J. B* **5** 423–438 (1998).

[81] M. Fogelström, S. Yip, and J. Kurkijärvi. "Pinhole junctions in d-wave superconductors." *Physics C* **294** 289–301 (1998).

[82] Y. S. Barash, H. Burkhardt, and D. Rainer. "Low-temperature anomaly in the Josephson critical current of junctions in d-wave superconductors." *Phys. Rev. Lett.* **77** 4070–4073 (1996).

[83] M. Fogelström and S. K. Yip. "Time-reversal symmetry-breaking states near grain boundaries between d-wave superconductors." *Phys. Rev. B* **57** 14060–14063 (1998).

[84] T. Löfwander, V. S. Shumeiko, and G. Wendin. "Time-reversal symmetry breaking at Josephson tunnel junction of purely d-wave superconductors." *Phys. Rev. B* **62** 14653–14656 (2000).

[85] Y. Tanaka. "Josephson effect between s wave and $d_{x^2-y^2}$ wave superconductors." *Phys. Rev. Lett.* **72** 3871–3874 (1994).

[86] S. Östlund. "Landau Ginzberg theory of the d-wave Josephson junction." *Phys. Rev. B* **58** 14757–14758 (1998).

[87] S. Yip. "Weak link between conventional and unconventional superconductors." *J. Low Temp. Phys.* **91** 203–218 (1993).

[88] K. K. Likharev and L. A. Yakobson. "Steady-state properties of superconducting bridges." *Sov. Phys. Tech. Phys.* **20** 950–954 (1976).

[89] A. Baratoff, J. A. Blackburn, and B. B. Schwartz. "Current-phase relationship in short superconducting weak links." *Phys. Rev. Lett.* **25** 1096–1099 (1970).

[90] A. Baratoff, J. A. Blackburn, and B. B. Schwartz. "Current-phase relationship in short superconducting weak links." *Phys. Rev. Lett.* **25** 1738 (1970).

[91] E. Il'ichev et al. "Nonsinusoidal current-phase relationship of grain boundary Josephson junctions in high-T_c superconductors." *Phys. Rev. Lett.* **81** 894–897 (1998).

[92] E. Il'ichev. "Peculiarities of radio frequency $YBa_2Cu_3O_{7-x}$ superconducting quantum interference device response with finite amplitude of the second harmonic in the current-phase relationship." *Appl. Phys. Lett.* **77** 3429–3431 (2000).

[93] E. Il'ichev et al. "Degenerate ground state in a mesoscopic $YBa_2Cu_3O_{7-x}$ grain boundary Josephson junction." *Phys. Rev. Lett.* **86** 5369–5372 (2001).

[94] J. R. Waldram and J. M. Lumley. "Direct measurements of the current-phase relation in superconducting weak links." *Revue De Physique Appliquée* **10** 7–10 (1975).

Vita

William K. Neils was born on June 3, 1974, in Suffern, New York. He attended Binghamton University, State University of New York majoring in physics. While at Binghamton University William studied thin-film diffusion in Si using the technique of differential scanning calorimetry in the laboratory of Professor Eric J. Cotts. During this time he was inducted into the Binghamton University chapter of the Phi Beta Kappa honors society. He graduated with honors in 1996 and was awarded the George E. Moore Award for Academic Achievement in Physics. His interests in condensed-matter physics led him to the University of Illinois at Urbana-Champaign where, in his second year, he joined the research group of Professor Dale J. Van Harlingen. William spent four years in this group studying the symmetry of the high temperature cuprate superconductors using Josephson interferometry.

Following graduation William will remain in Urbana as a Postdoctoral Researcher for approximately six months.